# Detecting industrial ammonia and ethylene point sources with the thermal bands of Landsat 8 and 9

Adriana Valverde[1*], Shanyu Zhou[1], Javier Roger[1,2], Itziar Irakulis-Loitxate[1], Javier Gorroño[1], Lulu Si[1] and Luis Guanter[1,3]

[1] Research Institute of Water and Environmental Engineering (IIAMA), Universitat Politècnica de València, Spain

[2] Institute of Environmental Physics (IUP), University of Bremen, Bremen, Germany

[3] Environmental Defense Fund, Amsterdam, Netherlands

* Corresponding author's email: avaligl@doctor.upv.es

**Abstract**

Industrial point sources of ammonia ($NH_3$) and ethylene ($C_2H_4$) are poorly constrained in current inventories, in part because satellites tend to offer either fine spatial detail or frequent revisits. We show that the two thermal-infrared bands of the Landsat 8 and 9 Thermal Infrared Sensor (TIRS), though built for land-surface monitoring, can detect and spatially resolve such plumes at 100 m resolution. Using a B10/B11 band-ratio method at five facilities in Iraq, Oman, the United Arab Emirates, and Saudi Arabia, we identified hundreds of plumes over 2021–2025 that recur in most months, pointing to persistent rather than sporadic emission. Because TIRS cannot spectrally separate the two gases, we attribute them from the known source type, corroborated by IASI and hyperspectral cross-checks: Landsat detections agree with morning IASI overpasses on two-thirds to three-quarters of co-observed days, and a near-simultaneous EMIT overpass over the Iraq fertilizer plant confirms that the band-ratio signal follows genuine $NH_3$ enhancements. Crucially, Landsat resolves individual units that IASI blends into a single column, and its open, multi-decade archive reconstructs facility-level emission histories, with plumes traceable back to 2015, complementing hyperspectral imagers and pointing toward routine, facility-scale monitoring.

**Keywords**

Ammonia emissions, ethylene emissions, Landsat 8-9, TIRS bands

**Introduction**

Reactive trace gases emitted from agriculture and industry play a disproportionate role in degrading air quality and disturbing biogeochemical cycles. However, emissions from localized point sources are still underestimated in current inventories and observation systems[1]. Two of these gases, ammonia ($NH_3$) and ethylene ($C_2H_4$), are released from industrial sites and have been difficult to detect at the spatial scales of atmospheric satellites until now[2,3].

Ammonia is a pungent gas that occupies a central place in the global nitrogen cycle [4,5]. With an atmospheric lifetime of hours to days, it is the primary gaseous base, neutralizing acidifying compounds such as $SO_2$ and $NO_x$ to form secondary inorganic aerosols, a major component of fine particulate matter ($PM_{2.5}$). $PM_{2.5}$ inhalation is associated with cardiovascular and respiratory illness, while its deposition drives ecosystem acidification, eutrophication, and biodiversity decline[3,5–7]. Agriculture dominates the global budget (often >85% of emissions), distributed diffusely across cropland and pasture [8]. In comparison, non-agricultural sources account for only 5–15%, including industry, power plants, and transport (~4–5% combined)[8,9]. Unlike diffuse agricultural emissions, industrial $NH_3$ is released from localized, high intensity point sources such as fertilizer plants, where large quantities are emitted from a single, identifiable location. Conventional $NH_3$ production is highly fossil-fuel-dependent, accounting for roughly 2% of global energy use and emitting about 450 Mt of carbon dioxide ($CO_2$) per year[10].

On the other hand, ethylene is a organic gas naturally produced by plants and soil microorganisms (Luttrell & Fletcher, 2016). As a highly reactive volatile organic compound with a lifetime of hours to days, it degrades rapidly via hydroxyl radicals and is an efficient precursor to tropospheric ozone and formaldehyde, posing risks to health and ecosystems [2,11]. Natural ethylene comes from biomass burning and natural biogenic processes. Additionally, anthropogenic ethylene emissions originate from petrochemical facilities, steel and coal-related industries, and fuel combustion [2,11], with the global ethylene industry emitting ~260 Mt $CO_2$ per year [12]. As with ammonia, much of this comes from identifiable industrial point sources, making it well suited to facility-scale detection.

Over the past several years, satellite instruments such as the Infrared Atmospheric Sounding Interferometer (IASI)[2,3,13] and the Cross-track Infrared Sounder (CrIS) [14] have demonstrated the capacity to retrieve $NH_3$ columns at global scales. IASI has similarly been used to map $C_2H_4$: Franco et al. (2022) identified more than 300 global hotspots, of which 138 (41%) were associated with the chemical industry. The strength of these sounders lies in their frequent, near-global revisit, which makes them well-suited to routine monitoring; their coarse spatial resolution, however, limits their ability to resolve individual emission sources (see Figure 1). Airborne thermal-infrared instruments such as the Hyperspectral Thermal Emission Spectrometer (HyTES) have also shown that $NH_3$ point sources can be resolved at the meter-to-tens-of-meters scale, though only within the limited footprints of dedicated flight campaigns[15].

This limitation is now being addressed from a complementary perspective, leveraging reflected sunlight in the shortwave infrared (SWIR), where thermal contrast is not required

Recent studies have demonstrated ammonia plume mapping in this spectral region: Balasus et al. (2026) retrieve ammonia column enhancements at 30 m resolution from the Tanager-1 imaging spectrometer, while Roger et al. (2026a, 2026b) extended the approach across a broader fleet (EMIT, EnMAP, PRISMA, Gaofen-5A, MethaneSAT), deriving consistent, lifetime-corrected emission rates for ammonia and ethylene. Additionally, EMIT-based ammonia detection has already been shown by Růžička et al., 2026. Because these instruments sample numerous narrow, contiguous bands, they can attribute a plume to a specific gas based solely on its spectral fingerprint. Their decisive limitation, however, is temporal: revisit is sparse and largely task-dependent, so a source is sampled only occasionally. In parallel, the thermal infrared route has also been followed, though it is constrained by thermal contrast: plume radiance anomalies strengthen when surface and gas-layer temperatures differ, collapse near zero contrast, and can reverse sign when the gas layer is warmer[17,18]. Tijhuis et al. (2026) eveloped a physically based retrieval for ASTER, using its broad bands 13 and 14 to detect facility-scale $NH_3$ plumes at 90 m. These considerations motivate a cautious detection-oriented assessment for Landsat TIRS, where only two broad thermal bands are available and the $NH_3$/$C_2H_4$ split-window signals are not uniquely separable from the imagery alone.

The Landsat series of Earth observation satellites offers a compelling, albeit unconventional, avenue that bridges these two approaches, combining a spatial resolution fine enough to resolve individual facilities with a revisit frequency and archive depth that the SWIR instruments lack. Although originally designed for land-surface monitoring, the Thermal Infrared Sensor (TIRS) aboard Landsat 8 and Landsat 9 operates in two thermal-infrared bands spanning roughly 10.6-11.2 µm (band 10) and 11.5-12.5 µm (band 11), spectral regions that overlap with known absorption features of both $NH_3$ and $C_2H_4$ (Figure 1). Combined with a 100 m sampling (resampled to 30 m), an 8-day revisit is achieved when both satellites operate concurrently, and a freely accessible archive spanning more than one decade, Landsat presents a unique opportunity for the retrospective and ongoing detection of these gases at spatial scales previously inaccessible from orbit.

This letter shows the feasibility of exploiting Landsat thermal-infrared observations to detect $NH_3$ and $C_2H_4$, examines the spectral and physical basis for the approach, and presents results from regions with known emission sources.

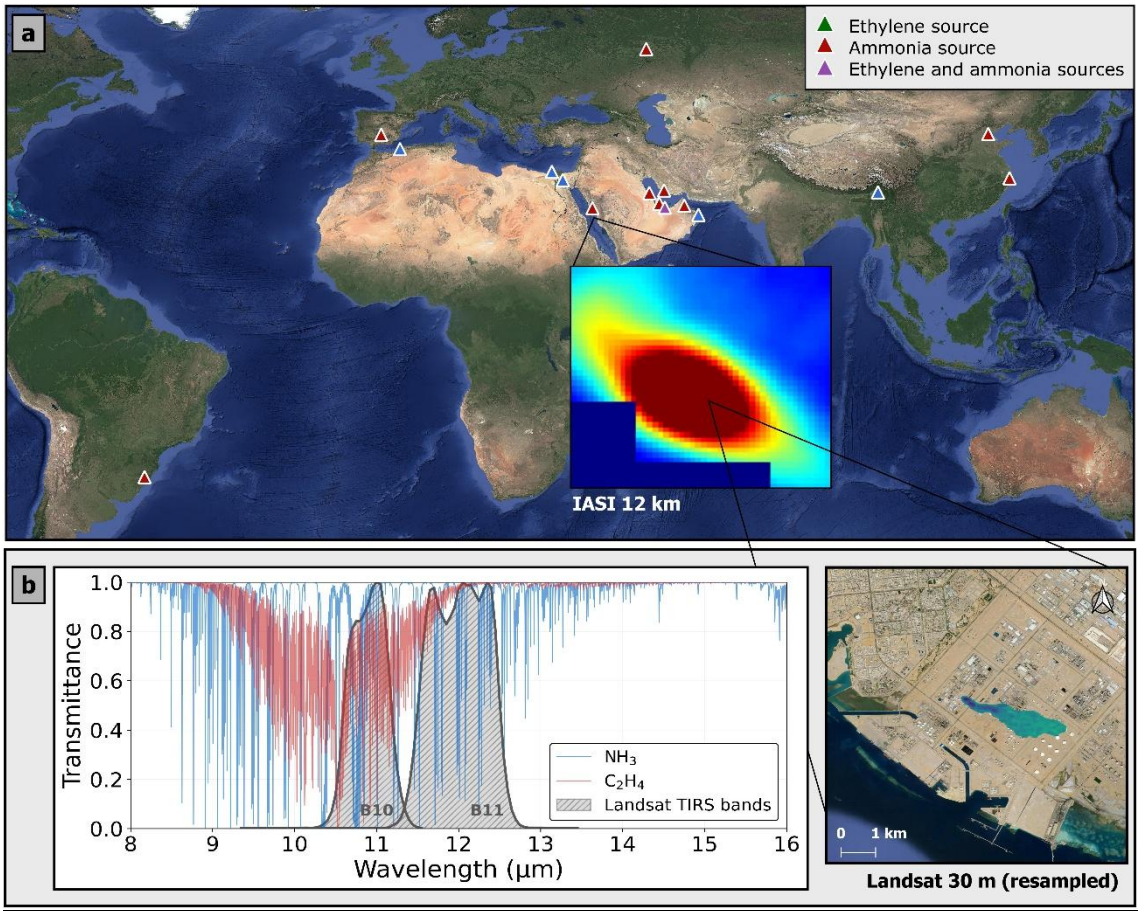


**Figure 1.** Industrial $NH_3$ and $C_2H_4$ point sources and the spectral basis for their detection with Landsat. (a) Global distribution of the facilities where Landsat detected at least one plume over 2021–2025, coloured by target gas: ethylene sources (red), ammonia sources (blue), and the site emitting both gases (purple). The insets contrast the two instruments over a single ethylene source in Saudi Arabia: the IASI panel (centre) shows the emission integrated into a single ~12 km footprint, derived from an oversampled average of ten years of IASI observations (Franco et al., 2022), whereas Landsat resolves the same plume at 30 m on 11 April 2022, tracing it to the individual facility (right). Basemap and Landsat inset: Google Satellite. (b) Atmospheric transmittance spectra of $NH_3$ (blue) and $C_2H_4$ (red), with the two Landsat TIRS channels (B10 and B11) shaded. Both gases have strong absorption features overlapping B10: $NH_3$ peaking near 10.3-11 μm and $C_2H_4$ near 10.5 μm, which is the spectral basis for the B10/B11 band-ratio detection; the overlap of their features within the single broad B10 channel also explains why the two bands cannot, on their own, spectrally distinguish the two species.

## Methodology

### 1. Detection with Landsat

To detect $NH_3$ and $C_2H_4$ we used the satellite imagery from the Landsat 8-9 Level 1 [19]. Both Landsat 8 and Landsat 9, launched in 2013 and 2021 respectively, share a common instrument design. Landsat 8's optical sensor, the Operational Land Imager (OLI), records reflectance from the visible through the shortwave-infrared, paired with the Thermal Infrared Sensor (TIRS); Landsat 9 carries refined counterparts, the OLI-2 and the TIRS-2. In this study, we used the TIRS thermal bands (B10 and B11). TIRS is a thermal imager operating in pushbroom mode with two infrared channels: Band 10 (centered at ~10.8 μm)

and Band 11 (centered at ~12 µm). These bands have a native 100-m resolution, resampled to 30 m to match the multispectral bands. The data were obtained through the Copernicus Data Space Ecosystem viewer [20].

To detect $NH_3$ and $C_2H_4$ emissions with Landsat 8-9, we adapted the multiband single-pass (MBSP) approach[21,22]. The detectability of a plume in the thermal infrared depends on thermal contrast, the temperature difference between the radiating surface and the cooler gas layer above it. Absorption by $NH_3$ or $C_2H_4$ reduces the upwelling radiance in B10 only when this contrast is present; over hot, dry surfaces the contrast is large and stable, enhancing the near-source signal, whereas it weakens or reverses when surface and plume temperatures converge. This dependence is well established for thermal point-source detection, from airborne hyperspectral imaging [23] to recent facility-scale ammonia retrievals from multispectral thermal data [24], and it explains why the semi-arid coastal sites examined here are favorable for detection. For this reason, the Landsat 8-9 plumes were detected by applying the B10/B11 band ratio for each image (more information in Text S1 and Figure S1). The band ratio reveals that an absorbing gas is present, but the two broad TIRS bands cannot resolve its spectral identity, so the method itself does not distinguish $NH_3$ from $C_2H_4$. We therefore attribute the emission based on the known source type. Although $NH_3$ and $C_2H_4$ can be released by several types of facilities, in this study, we detected plumes only at fertilizer plants, which we attribute to $NH_3$, and at petrochemical facilities, which we attribute to $C_2H_4$.

**2. Validation with hyperspectral data**

To confirm that the thermal anomalies detected by Landsat correspond to genuine $NH_3$ plumes, we compared a Landsat acquisition against a near-simultaneous EMIT observation of the same source. EMIT is a spaceborne imaging spectrometer [25,26] that retrieves $NH_3$ concentrations directly from its shortwave-infrared absorption features using a matched-filter method; the EMIT $NH_3$ retrieval used here is the one reported for an Iraq fertilizer plant in Roger et al. (2026). For that same plant, we identified a Landsat overpass acquired only 28 minutes apart from the EMIT scene (25 August 2023), allowing a near-coincident comparison between the two instruments. We then evaluated the spatial agreement between the Landsat band-ratio anomaly and the EMIT $NH_3$ column to test whether the broadband thermal anomaly scales with the $NH_3$ column densities retrieved by a dedicated hyperspectral instrument (see more information in Text S1).

**3. Validation with IASI**

We validated Landsat detections against IASI observations. IASI is a nadir-viewing thermal-infrared sounder with a 12 km nadir footprint that provides near-global coverage twice daily[27]. Because our detections span 2021–2025, we used only MetOp-B and MetOp-C and for all study locations, we retained only the morning (≈09:30 Land Solar Time) overpasses, which are closest in time to the Landsat acquisitions[28]. For both gases, we used the dimensionless hyperspectral range index (HRI) as the detection metric, which quantifies the strength of the target gas spectral signature relative to the gas-free atmospheric background (Clarisse et al., 2023; Franco et al., 2022). For $NH_3$, the HRI was taken directly from the IASI Level 2 $NH_3$ product v4.0.0 (Clarisse et al., 2023). For $C_2H_4$, no operational Level 2 product exists, so the HRI was computed from the Level 1C radiance spectra following Franco et al. (2022), using the processing code made publicly available by the authors. In both cases, for each site and date we retained the cloud-free pixel with the

largest absolute HRI within a fixed radius of the source, flagged a detection when HRI > 3, and selected the IASI acquisition closest to the Landsat overpass time. The HRI is constructed to have zero mean and unit standard deviation over gas-free background spectra [29], so a threshold of HRI > 3 corresponds to a 3σ enhancement above the background. We adopted this conservative cut to minimize false positives while remaining sensitive to genuine plumes. Full details of the data acquisition, quality screening, and processing are given in the Supporting Information (Text S2). For every detection, we have obtained wind speed using the ERA-5 repository [30]. Because we are uncertain about the effective height of the facilities, we examined wind speed at both 10 m and 100 m.

## Results

We began with a candidate set of 18 facilities previously reported as $NH_3$ or $C_2H_4$ sources [3,2,16,24,31,32]. Although we detected plumes in all these locations (see Table S1 and Figure S1), we concentrated the deep evaluation on the five facilities with the most detections (Figure S2): the fertilizer plant of Iraq (30.185, 47.838), the fertilizer plan of Oman (22.640, 59.428) for $NH_3$; the two petrochemical plants in Oman (24.491, 56.605) and in Saudi Arabia (23.979, 38.242) for $C_2H_4$; and the mixed fertilizer-petrochemical complex of the United Arab Emirates (24.126, 52.759), where both gases are emitted from adjacent facilities. All five lie in semi-arid coastal settings whose strong, stable surface thermal contrast makes a near-source thermal anomaly easier to detect than in other places.

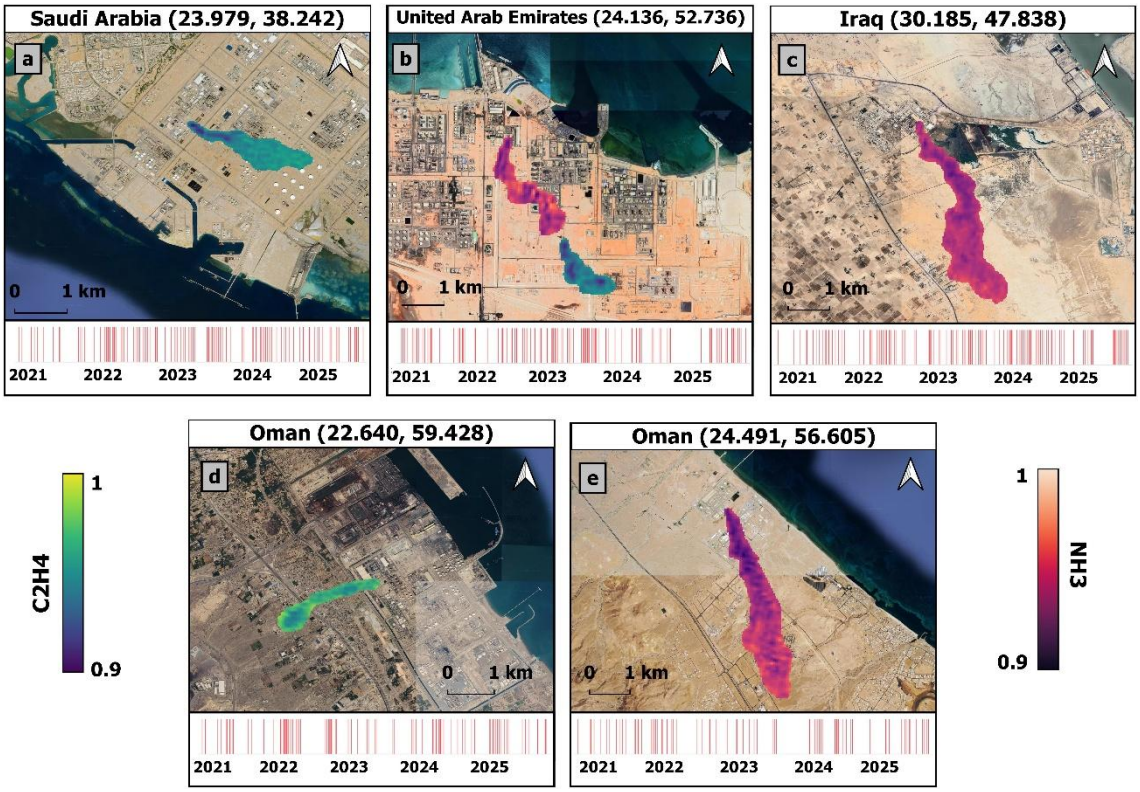


**Figure 2.** Landsat $NH_3$ and $C_2H_4$ plumes at the five focus facilities, with their detection time series represented by each red vertical line. Each panel shows a Landsat band-ratio plume overlaid on a Google Satellite basemap, with the 2021–2025 detection time series (red marks indicating days with a detected plume) below: (a) the Saudi Arabia petrochemical plant (23.979, 38.242), 2023-09-28; (b) the UAE fertilizer–petrochemical complex (24.136, 52.736), 2023-03-22; (c) the Iraq fertilizer plant

(30.185, 47.838), 2023-09-10; (d) the Oman fertilizer plant (22.640, 59.428), 2024-08-26; (e) the Oman petrochemical plant (24.491, 56.605), 2025-04-25. $C_2H_4$ plumes follow the green color scale, and $NH_3$ plumes the red scale.

The Iraqi fertilizer plant south of Khor Al-Zubair is both our richest record and the anchor for physical validation, having been the main case studied in Roger et al., 2026. Of 143 Landsat acquisitions inspected, 102 ammonia plumes were detected between January 2021 and December 2025 (Figure S3). In this case, the Landsat detections agree with IASI morning acquisitions in roughly 70% of cases (see Figure S4). To assess whether wind dispersion or satellite overpass timing explains cases in which IASI reported $NH_3$ but Landsat did not, we analyzed wind speed and the acquisition schedules of both sensors. Plumes at this facility are detectable at both low and high wind speeds (Figure S5), indicating that wind alone does not prevent detection. Instead, the temporal mismatch between the two overpasses accounts for much of the remaining disagreement (Figure S6). In about 90% of coincident detections, the two overpasses occur less than one hour apart, as expected. Conversely, when Landsat captures a plume but IASI does not, fewer than 50% of these instances occur within one hour, suggesting that emissions may have ceased before the IASI overpass. For cases in which IASI records a high $NH_3$ value while Landsat shows no plume, the overpasses are always within one hour of each other; however, these IASI values generally lie close to the detection threshold (HRI ≈ 3). In addition, we should note that Landsat plumes are visually identified, so in some cases, a faint plume may be present but not readily apparent. Despite this caveat, the persistence record (Figure S7) shows the Iraq facility as the most continuous source in this study, emitting in nearly every month of 2021–2025 with long-lived (≥1 h) plumes recurring throughout, so it can therefore be said that this source emits consistently over hours and days.

Independent confirmation that the thermal signal corresponds to genuine $NH_3$ emissions is provided by a near-simultaneous EMIT overpass on 25 August 2023 (Roger et al., 2026), when Landsat and EMIT imaged the plant only 28 minutes apart (07:22 and 07:50 UTC). EMIT was chosen for this comparison because, among the full set of hyperspectral imaging spectrometers that observed this facility (EMIT, EnMAP, PRISMA, Gaofen-5A, and MethaneSAT) it provides the only acquisition coincident with a Landsat overpass on the same day (Figure S8) The remaining sensors, although they detect the same persistent source, are offset from the nearest Landsat scene by one or more days, a separation too large for a plume that evolves over minutes to hours, and therefore cannot support a near-coincident comparison. For the EMIT scene, we evaluated the spatial agreement between the Landsat band-ratio anomaly and the EMIT $NH_3$ column, obtaining a strong linear correlation ($r = +0.85$; see Supporting Information, Text S2 and Figure S9). This agreement provides independent evidence that our Landsat method identifies genuine $NH_3$ plumes, and it establishes a proxy-to-concentration relationship for this source without requiring radiative-transfer simulations.

Among the five main facilities, the Oman fertilizer plant provides the lowest Landsat detection frequency. Across 145 Landsat acquisitions, we identified 62 $NH_3$ plumes (Figure S10). Agreement with IASI morning overpasses reached 66%, comprising 25 joint detections and 15 IASI-only detections (Figure S11). Notably, all Landsat plumes occurred at wind speeds below 4 m/s; above this threshold, no plumes were visible, consistent with stronger winds dispersing the emission before it can accumulate into a detectable plume

(Figure S12). At this site, joint detections exhibited overpass separations of less than one hour in 88% of cases, matching the expected temporal signature of a persistent source. Conversely, when IASI reported $NH_3$ but Landsat yielded no plume, only about half of the overpasses fell within one hour, suggesting that emissions began or ceased between the two acquisitions rather than indicating a failure of the Landsat retrieval method (Figure S13).

Moving to ethylene, the Oman petrochemical plant is the cleanest $C_2H_4$ case. Of 121 acquisitions, 69 plumes were detected (Figure S14), and across the subset of days with both a usable Landsat scene and a valid IASI retrieval, the two instruments agree 74% of the time at HRI > 3 (Figure S15). The timing scatter captures both extremes of that behavior: on 30 May 2021 and 15 June 2021, the sensors were more than two hours apart, yet both caught the plume, implying that the source emitted continuously for several hours, whereas on 26 February 2025, Landsat saw a plume that IASI missed despite a sub-hour gap, implying an emission that began and ended within the window. These two regimes are not isolated events but the visible endmembers of a generally persistent source: the monthly persistence record (Figure S8) shows this plant emitting in most months across 2021–2025, with the long-lived (≥1 h) plumes that survive the inter-overpass interval recurring throughout the series rather than clustering in any single period.

The Saudi Arabian petrochemical plant illustrates a clear case where Landsat resolves two distinct plume sources, whereas IASI registers them as a single column-integrated hotspot. Across 165 acquisitions, Landsat detected 97 ethylene plumes (59%), including 34 days (21%) on which both sources produced visible plumes simultaneously (Figure S18). Restricting the comparison to the 113 days with coincident, valid IASI retrievals, the two instruments agreed on 64 detections, while Landsat detected the plume alone on 8 days and IASI alone on 41 days (Figure S19). Consistent with the patterns observed at the other sites, plumes are detected at all wind speeds, and joint detections exhibited the highest HRI values and overpass separations of less than one hour in 75% of cases. The distinguishing feature of this site is the large pool of IASI-only days: these are not attributable to overpass timing alone, as most IASI-only days occur within an hour of the Landsat overpass; rather, they coincide with markedly higher wind speeds, many exceeding 5 m/s and several surpassing 10 m/s, which disperse the ethylene plume too rapidly to generate a detectable near-source thermal anomaly, even though IASI continues to register the elevated downwind column (Figures S20 and S21).

Finally, the UAE complex is the most demanding case and the one where the two gases must be discussed together, because a fertilizer unit emitting $NH_3$ sits immediately beside a petrochemical unit emitting $C_2H_4$ and the two broad TIRS bands cannot spectrally separate them. Over 261 observations Landsat detected 117 $C_2H_4$ plumes (45%) but only 20 $NH_3$ plumes (8%), with 144 clear days (Figure S22). The $C_2H_4$ comparison with IASI reaches a 48.3% true-positive rate at 58.6% accuracy with a substantial joint-detection count (75 days). At this site, the core challenge is therefore not plume detection, but plume attribution, determining which of the two gases each plume represents. For this reason, we tested several cases to confirm that we can observe these two gases in this complex (see Figure 3). On 22 March 2023, Landsat captured both the fertilizer $NH_3$ plume and the petrochemical $C_2H_4$ plume simultaneously, and both IASI gases were strongly enhanced, with HRI values of about 31 and 10, respectively. On 13 June 2021, when only the $C_2H_4$ plume was present, IASI reported elevated $C_2H_4$ (HRI ≈ 13) but background $NH_3$ (HRI ≈ 2). On 5 December 2024, when only the $NH_3$ plume was present, the pattern reversed, with

enhanced $NH_3$ (HRI ≈ 6) against negligible $C_2H_4$ (HRI ≈ 2). That the matching gas responds in IASI, rather than both species rising indiscriminately over a busy industrial area, is the strongest evidence that the band ratio tracks the intended source unit rather than a co-located confounder. The overpass-timing scatter for the complex (Figure S25) reinforces this interpretation, with joint detections clustering at high HRI and short Δt, consistent with the patterns observed at the other sites and confirming that the source remains persistent. This persistence is long-standing: the Landsat archive at this complex extends well beyond our 2021–2025 window, with the earliest clearly identifiable $C_2H_4$ plume dating to 4 November 2015, a reminder that the freely available archive can extend facility-level emission histories far beyond the period examined here.

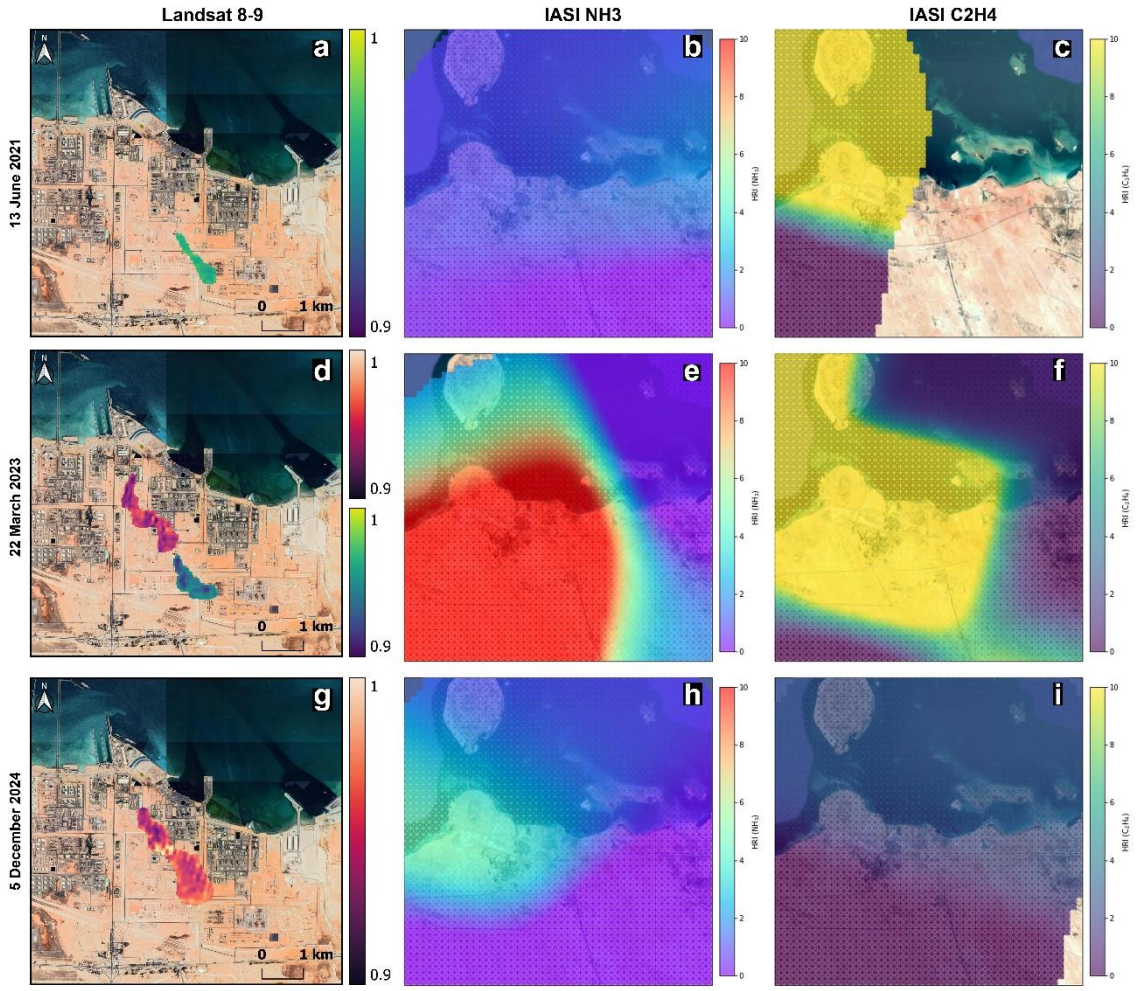


**Figure 3.** Co-located observations of pollution plumes over the United Arab Emirates complex (24.1369, 52.73659), on three dates: 13 June 2021 (a–c), 22 March 2023 (d–f), and 5 December 2024 (g–i). Each row pairs Landsat 8-9 imagery of the plume (left column) with IASI ammonia ($NH_3$) and ethylene ($C_2H_4$) hyperspectral range indices (HRI; middle and right columns). Top row (a–c), 13 June 2021: Landsat shows the $C_2H_4$ plume (a), alongside the IASI $NH_3$ (b) and $C_2H_4$ (c) HRI enhancements. Middle row (d–f), 22 March 2023: Landsat shows both the $NH_3$ and $C_2H_4$ plumes (d), with the corresponding $NH_3$ (e) and $C_2H_4$ (f) HRI enhancements. Bottom row (g–i), 5 December 2024: Landsat shows the $NH_3$ plume (g), with the $NH_3$ (h) and $C_2H_4$ (i) HRI fields. Landsat and IASI panels use Google Satellite imagery as a basemap.

Collectively, these five facilities illustrate the capability of Landsat 8-9 to provide consistent monthly detection records for all sources across the 2021–2025 period. None of the

sources is sporadic; emissions occur in most months of the record for every plant, with the Iraq and Saudi facilities showing the highest density, whereas the UAE complex proves the most intermittent: its $NH_3$ record is sparsely populated, indicating that its low ammonia yield reflects genuinely infrequent release rather than a detection failure. The central comparative result is that Landsat resolves individual stacks and adjacent units, which IASI necessarily blends, whereas IASI captures the dispersed downwind column that Landsat loses at high wind; the two instruments are thus complementary, and their disagreement is informative rather than indicative of a defect in either (Figure S26).

## Discussion

This study demonstrates that the thermal-infrared bands of Landsat 8 and 9, despite being designed primarily for land-surface monitoring, can detect and spatially resolve industrial $NH_3$ and $C_2H_4$ plumes at scales inaccessible to dedicated atmospheric sounders. Across five intensively analyzed facilities in Iraq, Oman, the UAE, and Saudi Arabia, a band-ratio method recovered hundreds of plumes over 2021–2025 and agreed with IASI on approximately two-thirds to three-quarters of co-observed days, with disagreements largely attributable to two well-understood mechanisms rather than to methodological failure: differences in overpass timing relative to intermittent emissions, and wind-driven dispersal of the near-source thermal anomaly.

Two capabilities distinguish Landsat from coarse-resolution sounders. First, its 100m resolution, resampled in 30 m, resolves individual sources that IASI merges into a single 12-km column. For instance, we could identify the two flare stacks at the Saudi site and the co-located $NH_3$ and $C_2H_4$ units in the UAE as emission point sources. Second, the freely available archive enables retrospective monitoring: at the UAE complex, a detectable plume is already present in 2015, well before our analysis window. Together, these capabilities allow Landsat to attribute emissions to specific facilities and to reconstruct their activity over time, complementing the daily, global view provided by TIR sounders.

However, the approach has clear limits. The two broad TIRS bands cannot spectrally distinguish $NH_3$ from $C_2H_4$, so attribution currently relies on known source type and on IASI cross-checking and with other hyperspectral satellites (Balasus et al., 2026, Roger et al., 2026); visual identification of plumes introduces subjectivity; and detection is sensitive to wind speed and to the surface thermal contrast that semi-arid sites happen to provide. These constraints define a natural agenda: automated, objective plume detection, explicit treatment of wind and thermal-contrast conditions, and the extension of cross-validation to more sites and both gases. The natural synergy is therefore one in which SWIR instruments calibrate and validate the emission signal, as our EMIT comparison illustrates, while the dense Landsat archive supplies the temporal continuity needed to turn isolated detections into emission histories.

For the same reasons, we deliberately restrict this study to detection and source attribution and do not attempt to quantify emission rates. Converting a thermal anomaly into a flux would require a physically based radiative-transfer inversion that is poorly constrained for the two broad TIRS bands: thermal contrast varies between scenes, the bands cannot isolate the target gas spectrally, and a single overpass captures only an instantaneous plume state. These difficulties are not unique to Landsat. Tijhuis et al. (2026), applying a

dedicated lookup-table retrieval over the same Iraq facility studied here, show that even a purpose-built multispectral thermal retrieval yields source rates that must be interpreted as instantaneous, successful-scene estimates rather than annual mean or continuous facility-average emissions, and conclude that such an approach is best suited to large, persistent sources and episodic plume mapping rather than to routine monitoring. Our objective is the complementary one. Rather than mapping episodic plumes, we use Landsat to build a regular, multi-year detection record, and the value of that record lies in its temporal continuity: an 8-day combined revisit and a freely available archive spanning more than a decade. We therefore report calibrated detections together with the hyperspectral-anchored proxy-to-concentration relationship established by the EMIT comparison and leave flux quantification to the SWIR imaging spectrometers and atmospheric sounders designed for it, with Landsat supplying the temporal backbone they lack.

The outlook is nonetheless favorable, because the next generation of thermal-capable missions will sharpen exactly the parameters that limit the present method. The Copernicus Land Surface Temperature Monitoring mission (LSTM), with a first launch planned for around 2028, will carry five thermal-infrared bands spanning roughly 8-12.5 µm at about 50 m spatial resolution and a revisit of one to a few days [34], a substantial improvement over the current Landsat 8-9 . Landsat Next (Landsat 10), targeted for late 2030/early 2031 as a three-satellite constellation, is designed to expand the thermal set from two to five bands, with the thermal bands at 60 m, and shorten the global revisit to about six days [35]. Finer spatial sampling and more frequent acquisition would directly reduce both the timing mismatch and the wind-dispersal blind spot identified here, while the additional thermal bands could potentially allow $NH_3$ and $C_2H_4$ to be spectrally separated rather than relying on source-type priors. Beyond these forthcoming missions, the same band-ratio principle could be tested on other thermal imagers already in orbit. The Visible Infrared Imaging Radiometer Suite (VIIRS), aboard the Suomi-NPP and NOAA-20/21 satellites, carries thermal bands at 10.76 µm (M15) and 12 µm (M16), and its daily global coverage could provide a complementary high-frequency screening layer [36]. Additionally, the ECOsystem Spaceborne Thermal Radiometer Experiment on Space Station (ECOSTRESS) provides five narrow thermal bands between 8 and 12.5 µm at roughly 70 m resolution, including a band centred at 10.49 µm that overlaps the $NH_3$ and $C_2H_4$ absorption features; its finer spectral sampling could, in principle, help to distinguish the two gases that the two broad Landsat bands cannot separate [37]. Moreover, because the method relies on thermal emission rather than reflected sunlight, it is not restricted to daytime overpasses in principle, and night-time thermal acquisitions could extend detection to hours when surface-atmosphere thermal contrast and emission behavior differ from the daytime case; exploring this possibility, where such observations are available, is a promising direction for future work. The scale of the archive also invites automation. Given the very large volume of freely available Landsat data, machine-learning methods could accelerate the systematic mining of the record and the reconstruction of historical emission patterns at these plants, mirroring their growing use in methane point-source monitoring. Taken together (the new thermal missions, the potential for day-and-night acquisition, and automated archive mining), the combination of the Landsat archive's long-term record and the enhanced spatial, temporal, and spectral resolution of the coming generation could make routine, facility-level monitoring of reactive-gas point sources a practical reality.

**Acknowledgment**

We thank NASA's Jet Propulsion Laboratory for the EMIT data, and the U.S. Geological Survey and its Earth Resources Observation and Science (EROS) Center, together with the Copernicus Data Space Ecosystem, for maintaining and freely distributing the Landsat 8–9 archive. We are grateful to EUMETSAT for the IASI Level 1C and Level 2 products aboard MetOp-B and MetOp-C. We acknowledge the Copernicus Climate Change Service for the ERA5-Land reanalysis, and to Google for the satellite basemap imagery used in the figures. This research is partly funded by the ESA MEDUSA project (ESA Contract No. 4000143908/24/I-LR) and the Spanish Ministry of Science, Innovation and Universities (Grant PID2023-148485OB-C21/C22 funded by MCIU/AEI/10.13039/501100011033 ERDF, EU). Itziar Irakulis-Loitxate is funded by UNEP's International Methane Emissions Observatory (IMEO).

**Code and data availability**

Landsat 8–9 Collection 2 Level-1 imagery is freely available from the U.S. Geological Survey (https://doi.org/10.5066/P975CC9B) and was accessed through the Copernicus Data Space Ecosystem (https://dataspace.copernicus.eu). The IASI Level 2 $NH_3$ product (v4.0.0) and the Level 1C radiance spectra used to compute the $C_2H_4$ HRI are distributed by EUMETSAT through its Data Store (https://data.eumetsat.int); the $C_2H_4$ retrieval code is available from Franco et al. (2022) at https://doi.org/10.5281/zenodo.7085725. ERA5-Land reanalysis wind fields are available from the Copernicus Climate Change Service Climate Data Store (https://doi.org/10.24381/CDS.E2161BAC).

**Competing interests**

The authors declare no competing interests.

**References**

(1) Dammers, E.; McLinden, C. A.; Griffin, D.; Shephard, M. W.; Van Der Graaf, S.; Lutsch, E.; Schaap, M.; Gainairu-Matz, Y.; Fioletov, V.; Van Damme, M.; Whitburn, S.; Clarisse, L.; Cady-Pereira, K.; Clerbaux, C.; Coheur, P. F.; Erisman, J. W. $NH_3$ Emissions from Large Point Sources Derived from CrIS and IASI Satellite Observations. *Atmos. Chem. Phys.* **2019**, *19* (19), 12261–12293. https://doi.org/10.5194/acp-19-12261-2019.

(2) Franco, B.; Clarisse, L.; Van Damme, M.; Hadji-Lazaro, J.; Clerbaux, C.; Coheur, P.-F. Ethylene Industrial Emitters Seen from Space. *Nat Commun* **2022**, *13* (1), 6452. https://doi.org/10.1038/s41467-022-34098-8.

(3) Van Damme, M.; Clarisse, L.; Whitburn, S.; Hadji-Lazaro, J.; Hurtmans, D.; Clerbaux, C.; Coheur, P.-F. Industrial and Agricultural Ammonia Point Sources Exposed. *Nature* **2018**, *564* (7734), 99–103. https://doi.org/10.1038/s41586-018-0747-1.

(4) Lakshmi, P. R.; Mohan, B.; Kang, P.; Nanjan, P.; Shanmugaraju, S. Recent Advances in Fluorescence Chemosensors for Ammonia Sensing in the Solution and Vapor Phases. *Chem. Commun.* **2023**, *59* (13), 1728–1743. https://doi.org/10.1039/D2CC06529K.

(5) Wang, S.; Nan, J.; Shi, C.; Fu, Q.; Gao, S.; Wang, D.; Cui, H.; Saiz-Lopez, A.; Zhou, B. Atmospheric Ammonia and Its Impacts on Regional Air Quality over the Megacity of Shanghai, China. *Sci Rep* **2015**, *5* (1), 15842. https://doi.org/10.1038/srep15842.

(6) Sutton, M. A.; Erisman, J. W.; Dentener, F.; Möller, D. Ammonia in the Environment: From Ancient Times to the Present. *Environmental Pollution* **2008**, *156* (3), 583–604. https://doi.org/10.1016/j.envpol.2008.03.013.
(7) Tang, Z.; Guo, J.; Zhou, J.; Yu, H.; Zhang, Y.; Wang, Y.; Lian, X.; Ye, J.; He, X.; Han, R.; Li, J.; Huang, S. The Impact of Short-Term Exposures to PM2.5 Components and the Modification Effects of Ozone on Daily Mortality. *Atmospheric Environment* **2025**, *362*, 121579. https://doi.org/10.1016/j.atmosenv.2025.121579.
(8) Jiang, J.; Stevenson, D. S.; Uwizeye, A.; Casu, F. A. M.; Tempio, G.; Falcucci, A.; Sutton, M. A. Global Warming Increases Ammonia Emissions and Reduces the Efficacy of Mitigation Actions. *Commun Earth Environ* **2026**, *7* (1), 398. https://doi.org/10.1038/s43247-026-03404-3.
(9) Zhang, X.; Sun, Y.; Gao, Y.; Wang, C.; Liang, X.; Lam, S. K.; Zhang, S.; Winiwarter, W.; Van Grinsven, H. J. M.; Sutton, M. A.; Chen, D.; Gu, B. Halving Global Ammonia Emissions with Cost-Effective Measures. *Nat Sustain* **2026**, *9* (2), 247–259. https://doi.org/10.1038/s41893-025-01723-5.
(10) Bora, N.; Kumar Singh, A.; Pal, P.; Kumar Sahoo, U.; Seth, D.; Rathore, D.; Bhadra, S.; Sevda, S.; Venkatramanan, V.; Prasad, S.; Singh, A.; Kataki, R.; Kumar Sarangi, P. Green Ammonia Production: Process Technologies and Challenges. *Fuel* **2024**, *369*, 131808. https://doi.org/10.1016/j.fuel.2024.131808.
(11) Dolan, W.; Payne, V. H.; Kualwik, S. S.; Bowman, K. W. Satellite Observations of Ethylene (C2H4) from the Aura Tropospheric Emission Spectrometer: A Scoping Study. *Atmospheric Environment* **2016**, *141*, 388–393. https://doi.org/10.1016/j.atmosenv.2016.07.009.
(12) Aui, A.; Moore, T.; Li, W.; Sarkar, A.; Duoss, E. B.; Hahn, C.; Baker, S. Net-Zero Ethylene: On the Sustainability, Economics, and Scalability of Synthetic and Fossil Production Pathways. *ACS Sustainable Chem. Eng.* **2025**, *13* (36), 14714–14725. https://doi.org/10.1021/acssuschemeng.5c02596.
(13) Clarisse, L.; Van Damme, M.; Clerbaux, C.; Coheur, P.-F. Tracking down Global $NH_3$ Point Sources with Wind-Adjusted Superresolution. *Atmos. Meas. Tech.* **2019**, *12* (10), 5457–5473. https://doi.org/10.5194/amt-12-5457-2019.
(14) Ding, J.; Van Der A, R.; Eskes, H.; Dammers, E.; Shephard, M.; Wichink Kruit, R.; Guevara, M.; Tarrason, L. Ammonia Emission Estimates Using CrIS Satellite Observations over Europe. *Atmos. Chem. Phys.* **2024**, *24* (18), 10583–10599. https://doi.org/10.5194/acp-24-10583-2024.
(15) Kuai, L.; Kalashnikova, O. V.; Hopkins, F. M.; Hulley, G. C.; Lee, H.; Garay, M. J.; Duren, R. M.; Worden, J. R.; Hook, S. J. Quantification of Ammonia Emissions With High Spatial Resolution Thermal Infrared Observations From the Hyperspectral Thermal Emission Spectrometer (HyTES) Airborne Instrument. *IEEE J. Sel. Top. Appl. Earth Observations Remote Sensing* **2019**, *12* (12), 4798–4812. https://doi.org/10.1109/JSTARS.2019.2918093.
(16) Růžička, V.; Thompson, D. R.; Fahlen, J. E.; Lopez, A. M.; Lu, S.; Xiang, C.; Bender, H.; Jensen, D.; Brodrick, P. G.; Lee, J.; Bue, B.; Cusworth, D. H.; Guanter, L.; Chlus, A.; Thorpe, A.; Green, R. O. Fully Automatic Trace Gas Plume Detection. arXiv 2026. https://doi.org/10.48550/ARXIV.2605.03372.
(17) Campion, R.; Salerno, G. G.; Coheur, P.-F.; Hurtmans, D.; Clarisse, L.; Kazahaya, K.; Burton, M.; Caltabiano, T.; Clerbaux, C.; Bernard, A. Measuring Volcanic Degassing of SO2 in the Lower Troposphere with ASTER Band Ratios. *Journal of Volcanology and Geothermal Research* **2010**, *194* (1–3), 42–54. https://doi.org/10.1016/j.jvolgeores.2010.04.010.
(18) Noppen, L.; Clarisse, L.; Tack, F.; Ruhtz, T.; Merlaud, A.; Van Damme, M.; Van Roozendael, M.; Schuettemeyer, D.; Coheur, P. Constraining Industrial Ammonia

Emissions Using Hyperspectral Infrared Imaging. *Remote Sensing of Environment* **2023**, *291*, 113559. https://doi.org/10.1016/j.rse.2023.113559.
(19) Earth Resources Observation and Science (EROS) Center. Landsat 8-9 Operational Land Imager / Thermal Infrared Sensor Level-1, Collection 2, 2013. https://doi.org/10.5066/P975CC9B.
(20) D.Kovács, D.; Musial, J.; Bojanowski, J.; Clarijs, D.; De La Mar, J.; Zlinszky, A. Copernicus Data Space Ecosystem Establishes Public Cloud Processing for Earth Observation Data. *Sci Data* **2026**, *13* (1), 537. https://doi.org/10.1038/s41597-026-06765-8.
(21) Varon, D. J.; Jervis, D.; McKeever, J.; Spence, I.; Gains, D.; Jacob, D. J. High-Frequency Monitoring of Anomalous Methane Point Sources with Multispectral Sentinel-2 Satellite Observations. *Atmos. Meas. Tech.* **2021**, *14* (4), 2771–2785. https://doi.org/10.5194/amt-14-2771-2021.
(22) Irakulis-Loitxate, I.; Guanter, L.; Maasakkers, J. D.; Zavala-Araiza, D.; Aben, I. Satellites Detect Abatable Super-Emissions in One of the World's Largest Methane Hotspot Regions. *Environ. Sci. Technol.* **2022**, *56* (4), 2143–2152. https://doi.org/10.1021/acs.est.1c04873.
(23) Hulley, G. C.; Duren, R. M.; Hopkins, F. M.; Hook, S. J.; Vance, N.; Guillevic, P.; Johnson, W. R.; Eng, B. T.; Mihaly, J. M.; Jovanovic, V. M.; Chazanoff, S. L.; Staniszewski, Z. K.; Kuai, L.; Worden, J.; Frankenberg, C.; Rivera, G.; Aubrey, A. D.; Miller, C. E.; Malakar, N. K.; Sánchez Tomás, J. M.; Holmes, K. T. High Spatial Resolution Imaging of Methane and Other Trace Gases with the Airborne Hyperspectral Thermal Emission Spectrometer (HyTES). *Atmos. Meas. Tech.* **2016**, *9* (5), 2393–2408. https://doi.org/10.5194/amt-9-2393-2016.
(24) Tijhuis, L. B.; Wizenberg, T.; Dammers, E. Facility-Scale Quantification and Monitoring of Ammonia ($NH_3$ ) Emissions Using ASTER Multispectral Thermal Infrared Observations. Gases/Remote Sensing/Data Processing and Information Retrieval June 16, 2026. https://doi.org/10.5194/egusphere-2026-2893.
(25) Connelly, D. S.; Thompson, D. R.; Mahowald, N. M.; Li, L.; Carmon, N.; Okin, G. S.; Green, R. O. The EMIT Mission Information Yield for Mineral Dust Radiative Forcing. *Remote Sensing of Environment* **2021**, *258*, 112380. https://doi.org/10.1016/j.rse.2021.112380.
(26) Green, R. EMIT L1B At-Sensor Calibrated Radiance and Geolocation Data 60 m V001, 2022. https://doi.org/10.5067/EMIT/EMITL1BRAD.001.
(27) Van Damme, M.; Whitburn, S.; Clarisse, L.; Clerbaux, C.; Hurtmans, D.; Coheur, P.-F. Version 2 of the IASI $NH_3$ Neural Network Retrieval Algorithm: Near-Real-Time and Reanalysed Datasets. *Atmos. Meas. Tech.* **2017**, *10* (12), 4905–4914. https://doi.org/10.5194/amt-10-4905-2017.
(28) Clerbaux, C.; Boynard, A.; Clarisse, L.; George, M.; Hadji-Lazaro, J.; Herbin, H.; Hurtmans, D.; Pommier, M.; Razavi, A.; Turquety, S.; Wespes, C.; Coheur, P.-F. Monitoring of Atmospheric Composition Using the Thermal Infrared IASI/MetOp Sounder. *Atmos. Chem. Phys.* **2009**, *9* (16), 6041–6054. https://doi.org/10.5194/acp-9-6041-2009.
(29) Clarisse, L.; Franco, B.; Van Damme, M.; Di Gioacchino, T.; Hadji-Lazaro, J.; Whitburn, S.; Noppen, L.; Hurtmans, D.; Clerbaux, C.; Coheur, P. The IASI $NH_3$ Version 4 Product: Averaging Kernels and Improved Consistency. *Atmos. Meas. Tech.* **2023**, *16* (21), 5009–5028. https://doi.org/10.5194/amt-16-5009-2023.
(30) Muñoz Sabater, J. ERA5-Land Hourly Data from 1950 to Present, 2019. https://doi.org/10.24381/CDS.E2161BAC.
(31) Roger, J.; Valverde, A.; Gorroño, J.; Pei, Z.; Irakulis-Loitxate, I.; Guanter, L. Remote Sensing of Ammonia Point Sources at High Spatial Resolution with Satellite-Based

Imaging Spectrometers. Atmospheric Sciences June 23, 2026. https://doi.org/10.31223/X5Q20M.
(32) Roger, J.; Valverde, A.; Gorroño, J.; Hilker, M.; Pei, Z.; Irakulis-Loitxate, I.; Guanter, L. Mapping Ethylene Plumes Using Satellite High-Resolution Imaging Spectrometers That Exploit the SWIR Spectrum. Environmental Monitoring June 30, 2026. https://doi.org/10.31223/X5K49G.
(33) Balasus, N.; Cusworth, D. H.; Kim, J.; Varon, D. J.; Miller, C. E.; Duren, R. M. Mapping Ammonia Emission Plumes Using Shortwave Infrared Imaging Spectroscopy. *Proc. Natl. Acad. Sci. U.S.A.* **2026**, *123* (24), e2605694123. https://doi.org/10.1073/pnas.2605694123.
(34) *LSTM*. https://sentiwiki.copernicus.eu/web/lstm (accessed 2026-06-22).
(35) *Landsat 10 | U.S. Geological Survey*. https://www.usgs.gov/landsat-missions/landsat-10 (accessed 2026-06-22).
(36) Cao, C.; De Luccia, F. J.; Xiong, X.; Wolfe, R.; Weng, F. Early On-Orbit Performance of the Visible Infrared Imaging Radiometer Suite Onboard the Suomi National Polar-Orbiting Partnership (S-NPP) Satellite. *IEEE Trans. Geosci. Remote Sensing* **2014**, *52* (2), 1142–1156. https://doi.org/10.1109/TGRS.2013.2247768.
(37) Fisher, J. B.; Lee, B.; Purdy, A. J.; Halverson, G. H.; Dohlen, M. B.; Cawse-Nicholson, K.; Wang, A.; Anderson, R. G.; Aragon, B.; Arain, M. A.; Baldocchi, D. D.; Baker, J. M.; Barral, H.; Bernacchi, C. J.; Bernhofer, C.; Biraud, S. C.; Bohrer, G.; Brunsell, N.; Cappelaere, B.; Castro-Contreras, S.; Chun, J.; Conrad, B. J.; Cremonese, E.; Demarty, J.; Desai, A. R.; De Ligne, A.; Foltýnová, L.; Goulden, M. L.; Griffis, T. J.; Grünwald, T.; Johnson, M. S.; Kang, M.; Kelbe, D.; Kowalska, N.; Lim, J.; Maïnassara, I.; McCabe, M. F.; Missik, J. E. C.; Mohanty, B. P.; Moore, C. E.; Morillas, L.; Morrison, R.; Munger, J. W.; Posse, G.; Richardson, A. D.; Russell, E. S.; Ryu, Y.; Sanchez-Azofeifa, A.; Schmidt, M.; Schwartz, E.; Sharp, I.; Šigut, L.; Tang, Y.; Hulley, G.; Anderson, M.; Hain, C.; French, A.; Wood, E.; Hook, S. ECOSTRESS: NASA's Next Generation Mission to Measure Evapotranspiration From the International Space Station. *Water Resources Research* **2020**, *56* (4), e2019WR026058. https://doi.org/10.1029/2019WR026058.

# Detecting industrial ammonia and ethylene point sources with the thermal bands of Landsat 8 and 9

**SUPPORTING INFORMATION**

Adriana Valverde[1*], Shanyu Zhou[1], Javier Roger[1,2], Itziar Irakulis-Loitxate[1], Javier Gorroño[1], Lulu Si[1] and Luis Guanter[1,3]

[1] Research Institute of Water and Environmental Engineering (IIAMA), Universitat Politècnica de València, Spain

[2] Institute of Environmental Physics (IUP), University of Bremen, Bremen, Germany

[3] Environmental Defense Fund, Amsterdam, Netherlands

* Corresponding author's email: avaligl@doctor.upv.es

**Contents of this file**



## Introduction

This supplementary material provides additional information on detecting ammonia and ethylene emissions using the TIRS bands of Landsat 8 and 9.

## METHODOLY

### Text S1. Validation with hyperspectral data.

To validate that the thermal anomalies detected by Landsat correspond to real $NH_3$ plumes, we used a near-simultaneous overpass from the EMIT imaging spectrometer, which retrieves $NH_3$ concentrations directly via matched-filter absorption features (Figure S9). On 25 August 2023, Landsat and EMIT observed an Iraq fertilizer plant within a 28-minute window (07:22 and 07:50 UTC, respectively). Both instruments independently detected an $NH_3$ plume extending downwind from the facility, with a ~13° offset in plume axis consistent with a wind direction shift between acquisitions. Because this angular offset precludes direct pixel-to-pixel comparison, we instead compared radial profiles along each sensor's own plume axis, binned every 50 m within a 0.5–2.0 km sampling window. The Landsat band-ratio anomaly (BR − BR_bg) was regressed against EMIT $NH_3$ column concentrations. BR_bg is defined as the median band ratio of all scene pixels located more than 3 km from the source, excluding water bodies (pixels below the 5th percentile of the scene band ratio). The strong linear correlation obtained using the 1500 nm whole matched-filter retrieval ($r = +0.85$, $p = 3.4 \times 10^{-9}$, $n = 30$) confirms that the signal captured by Landsat's thermal bands tracks actual $NH_3$ enhancements measured by a dedicated hyperspectral instrument. To assess the sensitivity of this result to methodological choices, we swept all seven EMIT $NH_3$ matched-filter bands across 21 radial integration windows. The band with the highest per-pixel signal-to-noise ratio, $NH_3$ 2300 nm (SNR = 2.14), yields $r = +0.67$ ($n = 20$); the difference in optimal window and correlation strength between bands likely reflects a combination of factors, including the 28-minute temporal gap between acquisitions, differences in per-pixel SNR, and the inherently different spectral sensitivities of each matched-filter configuration. A single matchup does not allow these contributions to be separated. This empirical agreement provides independent evidence that our Landsat-based detection method identifies genuine $NH_3$ plumes and establishes a proxy-to-concentration relationship for this source without requiring radiative transfer simulations.

### Text S2. Validation with IASI

We complemented the Landsat retrievals with IASI observations. IASI is a nadir-viewing Fourier-transform spectrometer that records the thermal-infrared spectrum emitted by the Earth–atmosphere system, covering the spectral range 645–2760 $cm^{-1}$ (3.7-15.5 μm) at a resolution of 0.5 $cm^{-1}$, with a 12 km nadir footprint (Van Damme et al., 2017). Its broad spectral coverage and low radiometric noise allow the retrieval of more than 30 atmospheric species, including $NH_3$ and $C_2H_4$. The instrument provides near-global coverage twice daily, with equator-crossing overpasses at approximately 09:30 and 21:30 local solar time (descending and ascending nodes) (Clerbaux et al., 2009). IASI flies aboard the three MetOp satellites: MetOp-A, MetOp-B, and MetOp-C, launched in 2006, 2012, and 2018, respectively. Because our detections are between 2021 and 2025, and the IASI instrument aboard MetOp-A was switched off in October 2021 (EUMETSAT, 2021), we used only the latter two platforms, MetOp-B and MetOp-C. For each of our five study locations, IASI provides both a morning and an evening overpass; we retained only the days with a morning (≈09:30 LST) overpass for both $NH_3$ and $C_2H_4$, since daytime observations are closer to Landsat acquisitions.

For $NH_3$, we used the IASI Level 2 $NH_3$ product (v4.0.0) from MetOp-B and MetOp-C (Clarisse et al., 2023). The retrieval is based on a dimensionless hyperspectral range index (HRI), which quantifies the strength of the $NH_3$ spectral signature and is subsequently converted to $NH_3$ columns through a neural network (Whitburn et al., 2016). In this work, we used the HRI directly as our detection metric. From each daily product, we extracted the geolocation, HRI, cloud coverage, and acquisition time, retained only finite, cloud-free pixels (cloud coverage ≤ 25%) falling within a fixed radius of each target's center, and took the pixel with the largest absolute HRI as the representative value for that location and date. A positive detection was flagged when the HRI exceeded a fixed threshold (HRI > 3). Because the HRI is normalized to have zero mean and unit standard deviation over gas-free background spectra (Van Damme et al., 2017; Clarisse et al., 2023), a value of HRI > 3 corresponds to a 3σ enhancement above the background, i.e. a signal that exceeds normal spectral variability with greater than 99% confidence; we therefore adopted HRI > 3 as our detection threshold. This is consistent with the common practice of thresholding the HRI to flag detections, although the exact cut is application-dependent—stricter values (e.g. HRI > 5) have been used elsewhere to isolate concentrated plumes (Franco et al., 2022). To align the IASI and Landsat observations in time, we selected the IASI acquisition closest to the Landsat overpass hour. Unlike $NH_3$, no operational Level 2 $C_2H_4$ product is distributed for IASI, so the ethylene HRI had to be computed directly from the Level 1C radiance spectra. We followed the approach of Franco et al. (2022), using the processing code made publicly available by the authors (Franco et al., 2022, Zenodo; https://doi.org/10.5281/zenodo.7085725), which computes the $C_2H_4$ HRI from IASI spectra and converts it into total columns using an artificial neural network. The HRI is a dimensionless quantity that measures the strength of the target gas absorption signature in each observed spectrum relative to the natural variability of the gas-free atmospheric background (Clarisse et al., 2023; Franco et al., 2022).

The input data were obtained programmatically from the EUMETSAT Data Store through its Python API (EUMDAC). For each study site and date, we queried the IASI Level 1C radiance products (MetOp-B/C) over a bounding box centered on the target and retained the pixels falling within a fixed radius of the source. Because the HRI-to-column conversion requires information on the atmospheric state, each Level 1C observation was paired with the temporally and spatially co-located IASI Level 2 sounding product, from which we extracted the temperature and water-vapor profiles together with the surface temperature and surface pressure of the matching pixel. Pixels were screened for completeness: observations were rejected when more than half of the radiance channels or a substantial fraction of the lower-tropospheric profile levels were missing, or when the surface variables were invalid. Residual gaps in the retained radiance spectra and profiles were filled by linear interpolation, and the temperature and water-vapor profiles were interpolated onto a fixed set of standard altitude levels. For each valid acquisition, the radiance spectrum and the associated auxiliary variables (surface temperature, surface pressure, emissivity, and the regridded profiles) were exported and supplied as input to the MATLAB HRI code of Franco et al. (2022), which returned the $C_2H_4$ HRI used in our analysis. Only morning overpasses were considered, and the acquisition closest in time to the Landsat overpass was selected.

## RESULTS

| Country | Lat | Lon | Facility | Gas | Nº of plumes |
|---|---|---|---|---|---|
| Saudi Arabia | 23.979 | 38.242 | Petrochemical | C2H4 | 97 |
| Saudi Arabia | 27.049 | 49.581 | Petrochemical | C2H4 | 29 |
| Brasil | -29.875 | -51.387 | Petrochemical | C2H4 | 3 |
| China | 38.819 | 117.406 | Petrochemical | C2H4 | 2 |
| China | 29.982 | 121.688 | Petrochemical | C2H4 | 1 |
| Iran | 27.555 | 52.552 | Petrochemical | C2H4 | 3 |
| Oman | 24.491 | 56.605 | Petrochemical | C2H4 | 69 |
| Qatar | 24.928 | 51.569 | Petrochemical | C2H4 | 3 |
| Spain | 38.673 | -4.049 | Petrochemical | C2H4 | 1 |
| Russia | 55.868 | 48.985 | Petrochemical | C2H4 | 2 |
| United Arab Emirates | 24.122 | 52.755 | Petrochemical | C2H4 | 97 |
| Argelia | 35.825 | -0.294 | Fertilizer | NH3 | 3 |
| Egypt | 29.628 | 32.297 | Fertilizer | NH3 | 12 |
| Egypt | 31.272 | 30.096 | Fertilizer | NH3 | 5 |
| India | 27.178 | 95.351 | Fertilizer | NH3 | 2 |
| Iraq | 30.186 | 47.837 | Fertilizer | NH3 | 102 |
| Oman | 22.637 | 59.428 | Fertilizer | NH3 | 62 |
| United Arab Emirates | 24.122 | 52.755 | Fertilizer | NH3 | 20 |

**Table S1. Facilities with Landsat plume detections, 2021–2025.** Location, gas, and number of detected plumes for each facility, ordered by gas. The five sources analyzed in detail: Saudi Arabia (23.979, 38.242), Oman (24.491, 56.605) and the UAE complex (24.122, 52.755) for $C_2H_4$, and Iraq (30.186, 47.837) and Oman (22.637, 59.428) for $NH_3$, are those with the highest plume detected.

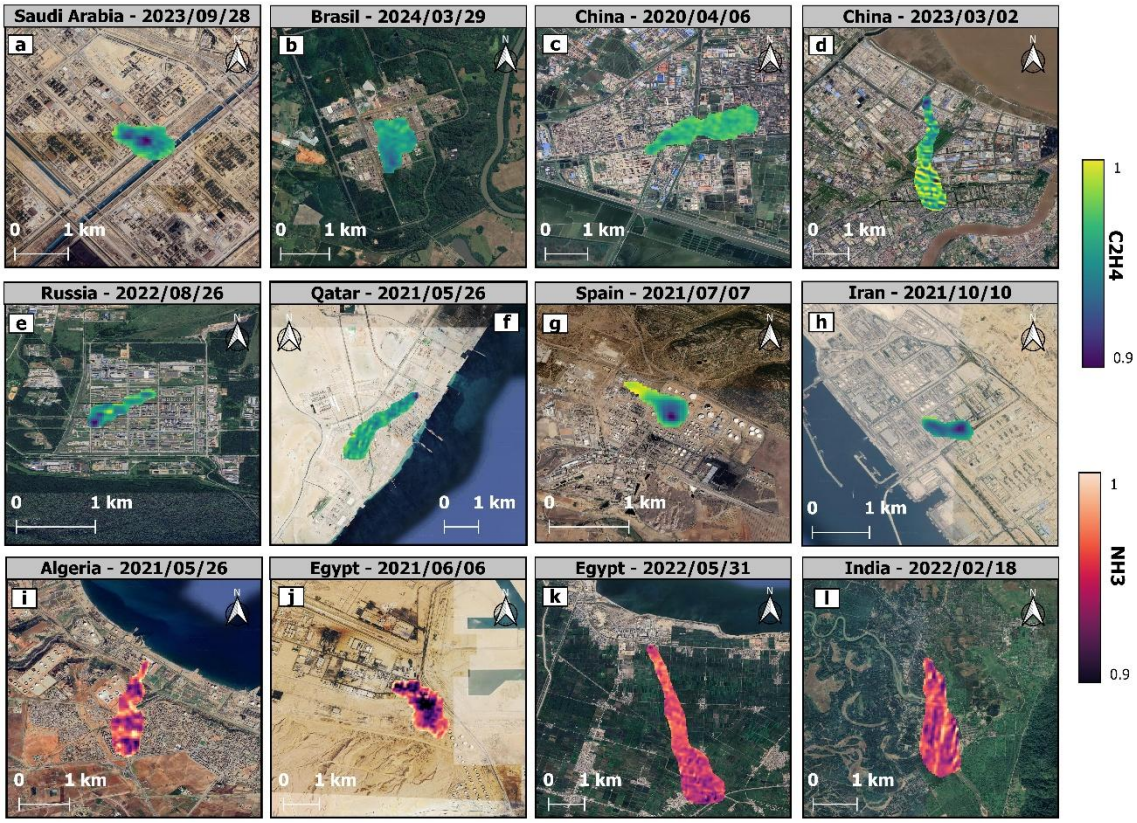


**Figure S1**. Examples of $NH_3$ and $C_2H_4$ plumes detected with Landsat 8-9. Landsat band-ratio plumes overlaid on Google Satellite basemaps for twelve further industrial sources, with acquisition dates indicated. $C_2H_4$ plumes (green colour scale): (a) Saudi Arabia, 27.049, 49.581 (2023-09-28); (b) Brazil, −29.875, −51.387 (2024-03-29); (c) China, 38.819, 117.406 (2020-04-06); (d) China, 29.982, 121.688 (2023-03-02); (e) Russia, 55.868, 48.985 (2022-08-26); (f) Qatar, 24.928, 51.569 (2021-05-26); (g) Spain, 38.673, −4.049 (2021-07-07); (h) Iran, 27.555, 52.552 (2021-10-10). $NH_3$ plumes (red color scale): (i) Algeria, 35.825, −0.294 (2021-05-26); (j) Egypt, 29.628, 32.297 (2021-06-06); (k) Egypt, 31.272, 30.096 (2022-05-31); (l) India, 27.178, 95.351 (2022-02-18).

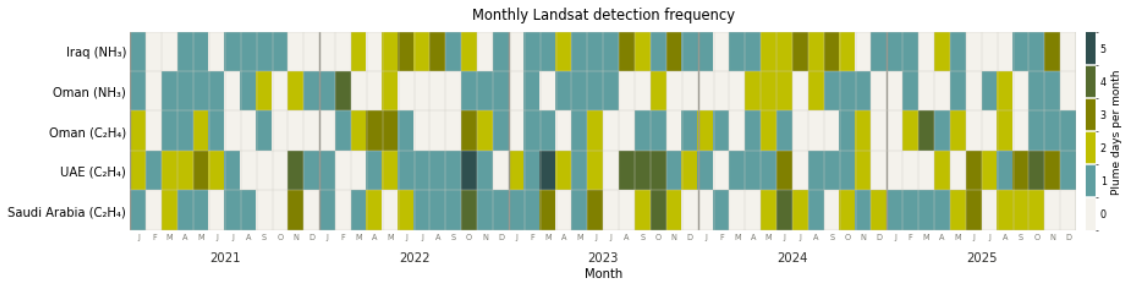


**Figure S2. Monthly Landsat detection frequency at the five focus facilities, 2021–2025.** Heatmap of the number of plume-detection days per month at each source: Iraq ($NH_3$), Oman ($NH_3$), Oman ($C_2H_4$), UAE ($C_2H_4$), and Saudi Arabia ($C_2H_4$). Color indicates the count of days with a detected plume in each month, from 0 (light) to 5 or more (dark), as shown by the color bar. The persistence of detections across most months indicates that all five sources are active throughout the record rather than emitting sporadically.

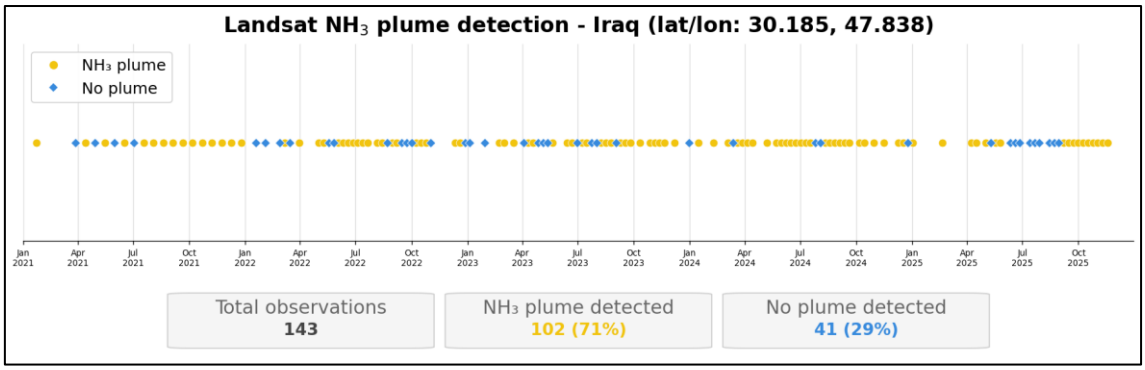


**Figure S3.** Detection timeline of all Landsat acquisitions between 2021-2025 in the Iraq fertilizer plant, marking plume and no-plume days.

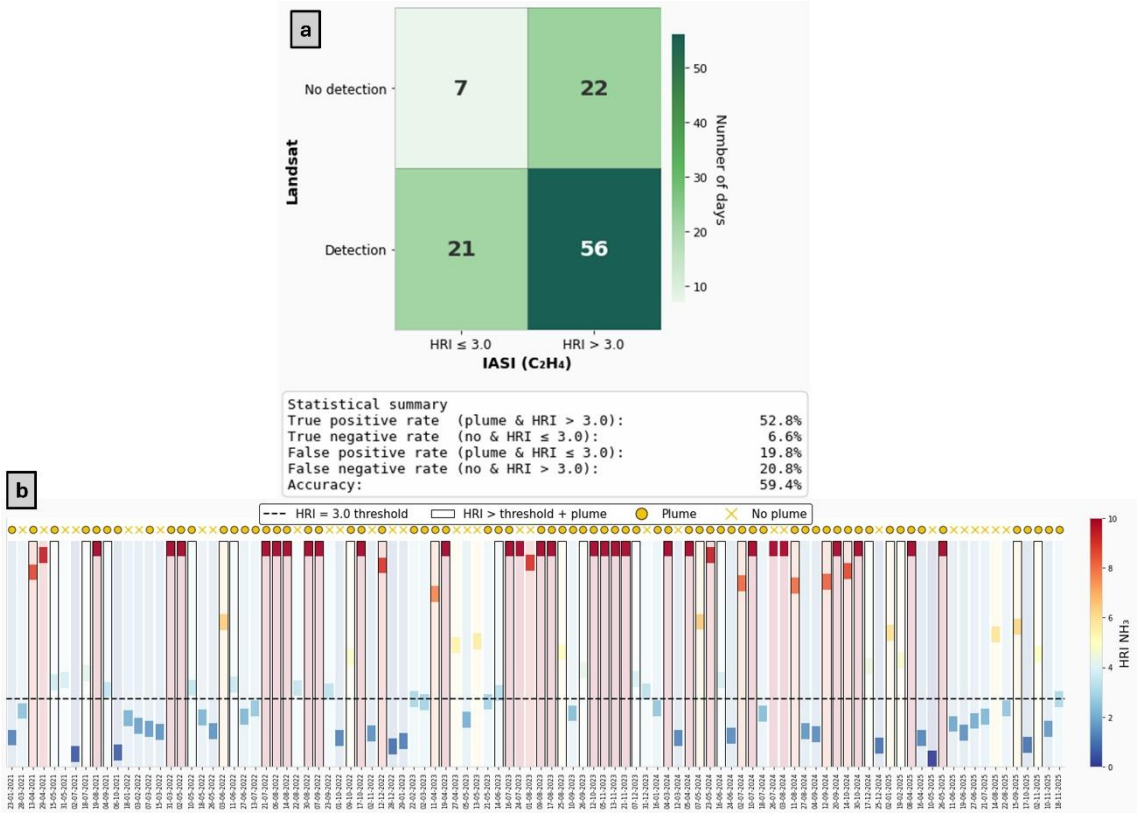


**Figure S4.** Landsat–IASI $NH_3$ comparison at the Iraq fertilizer plant. (a) Confusion matrix of the Landsat plume flag against the IASI threshold (HRI > 3), with the true-/false-positive rates and overall accuracy. (b) Per-day IASI $NH_3$ HRI relative to the HRI = 3 threshold, with Landsat plume/no-plume markers.

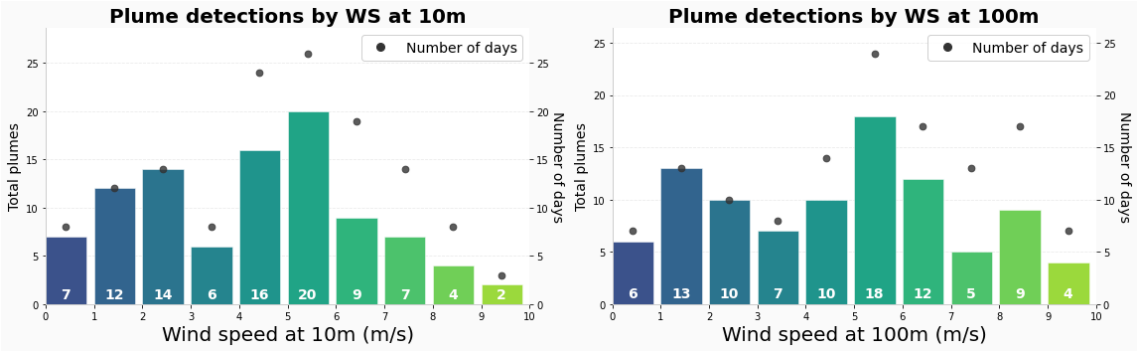


**Figure S5**. Plumes detected in the Iraq fertilizer plant under different wind speed conditions at 10 m and 100 m.

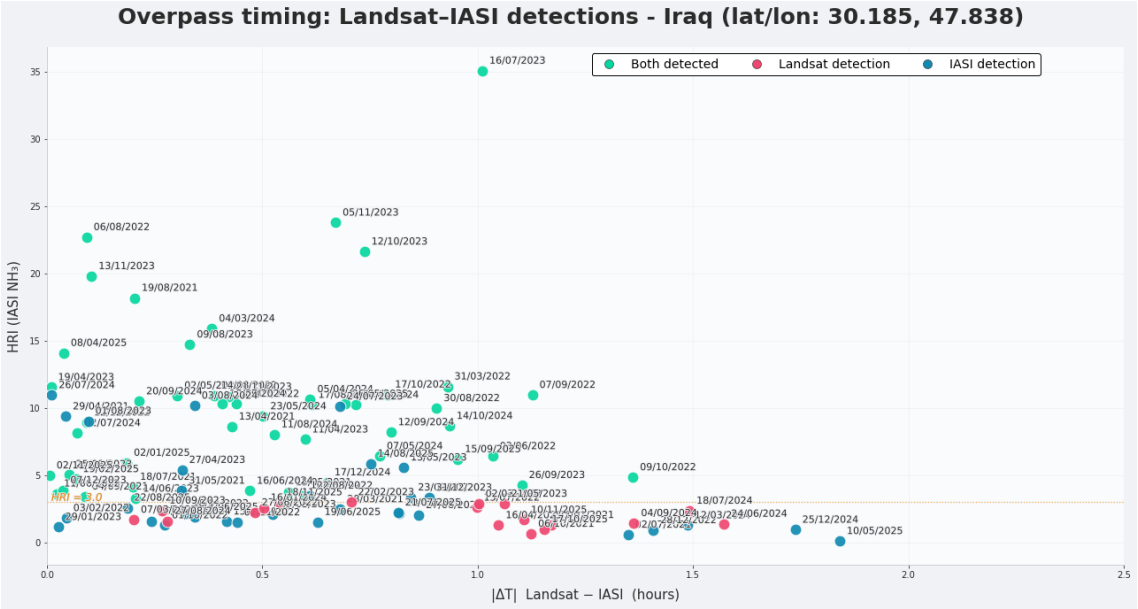


**Figure S6.** Scatter plot of IASI overpass timing versus the absolute Landsat-IASI time difference in the Iraq fertilizer plant. Points are colored according to detection status: both sensors, Landsat only, or IASI only.


**Figure S7.** Monthly detection persistence of the five focus sources, 2021–2025. Stacked monthly bar charts of detection days for, top to bottom, Iraq ($NH_3$), southern Oman ($NH_3$), northern Oman ($C_2H_4$), western Saudi Arabia ($C_2H_4$), and the UAE complex ($C_2H_4$). Plume longevity relative splits each bar to the inter-overpass interval: no plume, plume shorter than 1 h, and plume of 1 h or longer. The recurrence of long-lived (≥1 h) plumes indicates a persistent source rather than transient events.

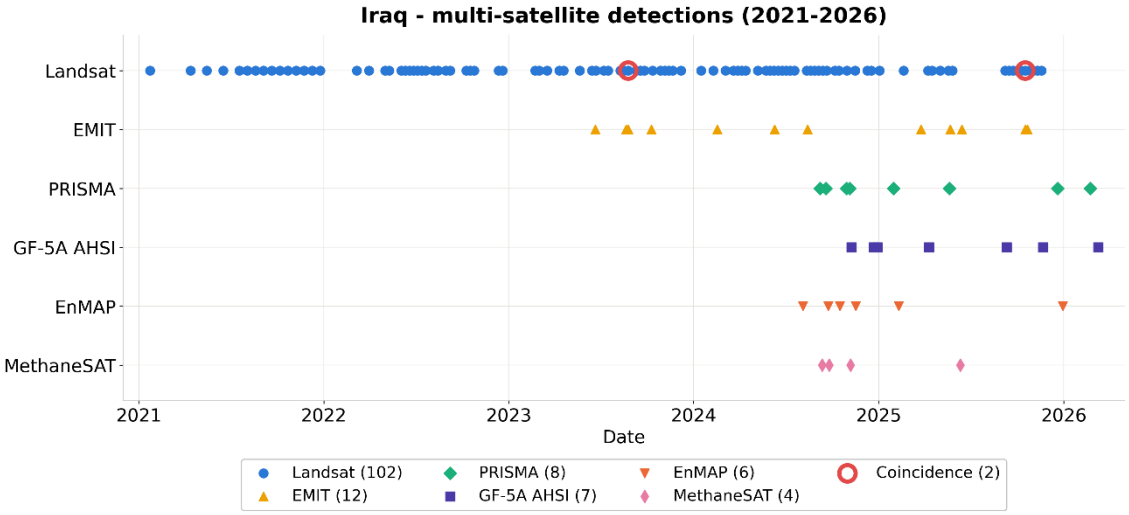


**Figure S8.** Temporal comparison between Landsat $NH_3$ plume detections and hyperspectral observations at the Iraq fertilizer plant (Khor Al-Zubair; 30.185, 47.838) reported by Roger et al. (2026). Landsat detection days over 2021–2025 are shown together with the acquisition dates of the hyperspectral imaging spectrometers (EMIT, EnMAP, PRISMA, Gaofen-5A, and MethaneSAT). Among all the hyperspectral acquisitions, only EMIT (25 August 2023 and 17 October 2025) coincides with a Landsat overpass on the same day.

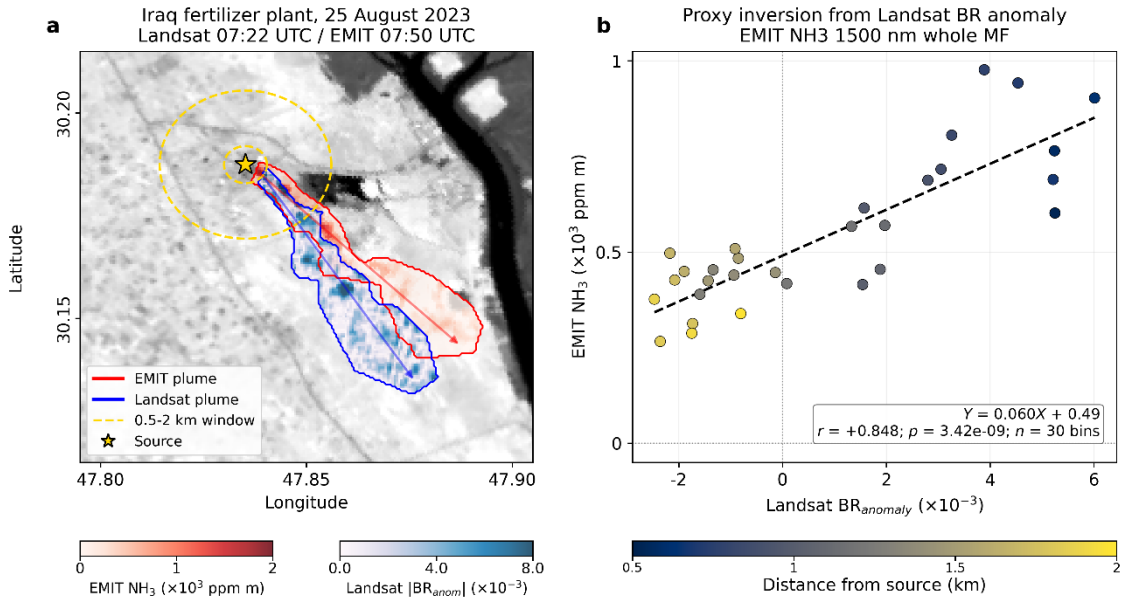


**Figure S9.** EMIT-Landsat cross-validation over the Iraq fertilizer plant (25 August 2023). Left: near-simultaneous Landsat (07:22 UTC) and EMIT (07:50 UTC; Δt = 28 min) views of the plume, with the radial sampling annuli (0.5-2.0 km) overlaid. Right: inversion of the EMIT $NH_3$ column (1500 nm whole-column matched filter) against the Landsat band-ratio anomaly (BR − BR_bg) in 50 m radial bins, giving r = +0.85 ($p = 3.4 \times 10^{-9}$, n = 30).

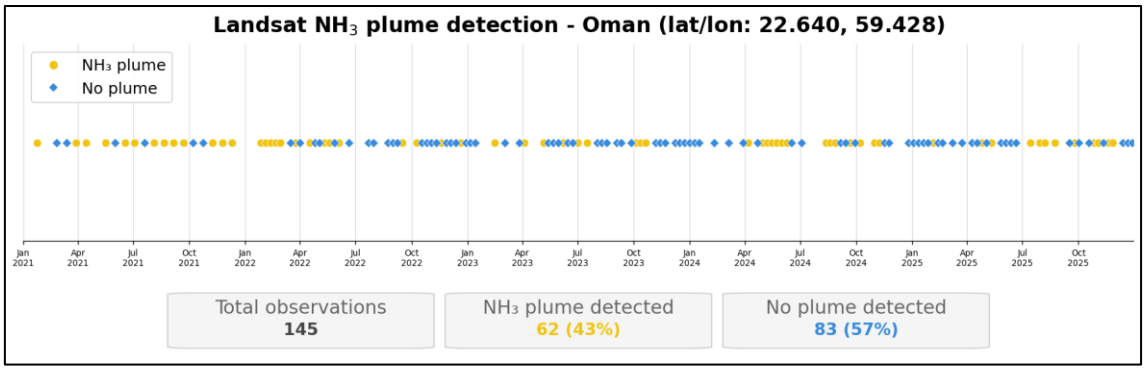


**Figure S10.** Detection timeline of all Landsat acquisitions between 2021-2025 in the Oman fertilizer plant, marking plume and no-plume days.

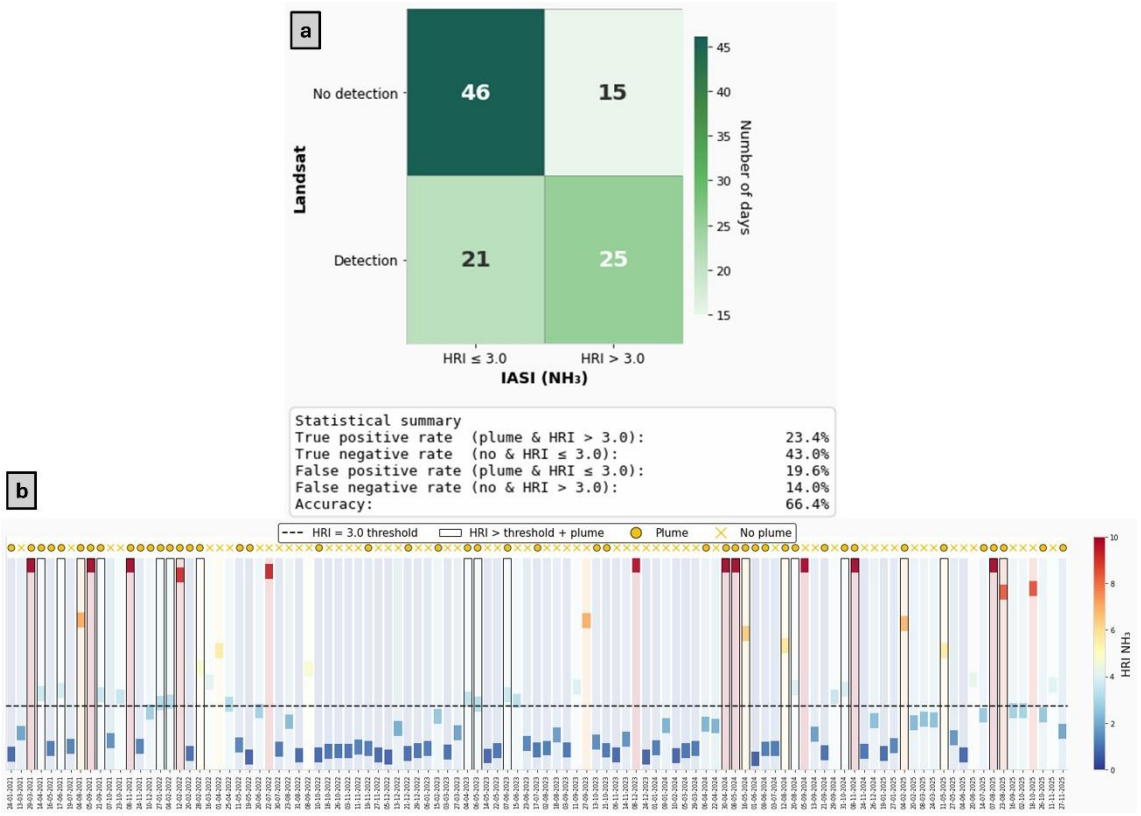


**Figure S11.** Landsat-IASI $NH_3$ comparison at the Oman fertilizer plant. (a) Confusion matrix of the Landsat plume flag against the IASI threshold (HRI > 3), with the true-/false-positive rates and overall accuracy. (b) Per-day IASI $NH_3$ HRI relative to the HRI = 3 threshold, with Landsat plume/no-plume markers.

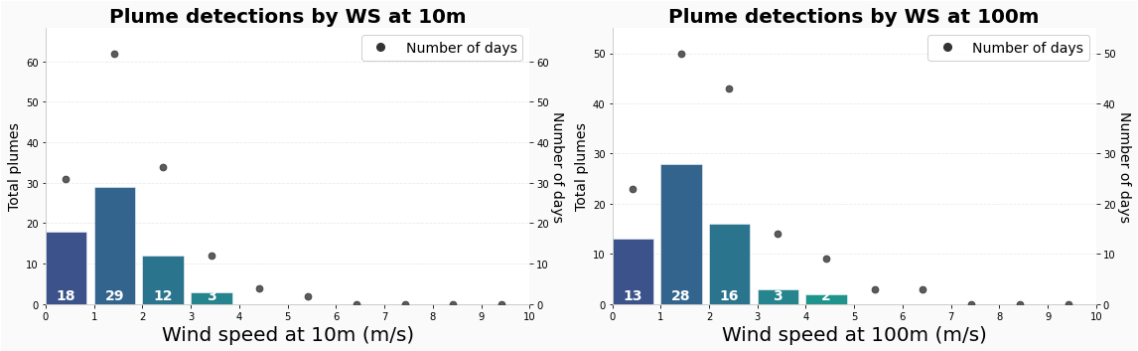


**Figure S12**. Plumes detected in the Oman fertilizer plant under different wind speed conditions at 10 m and 100 m.

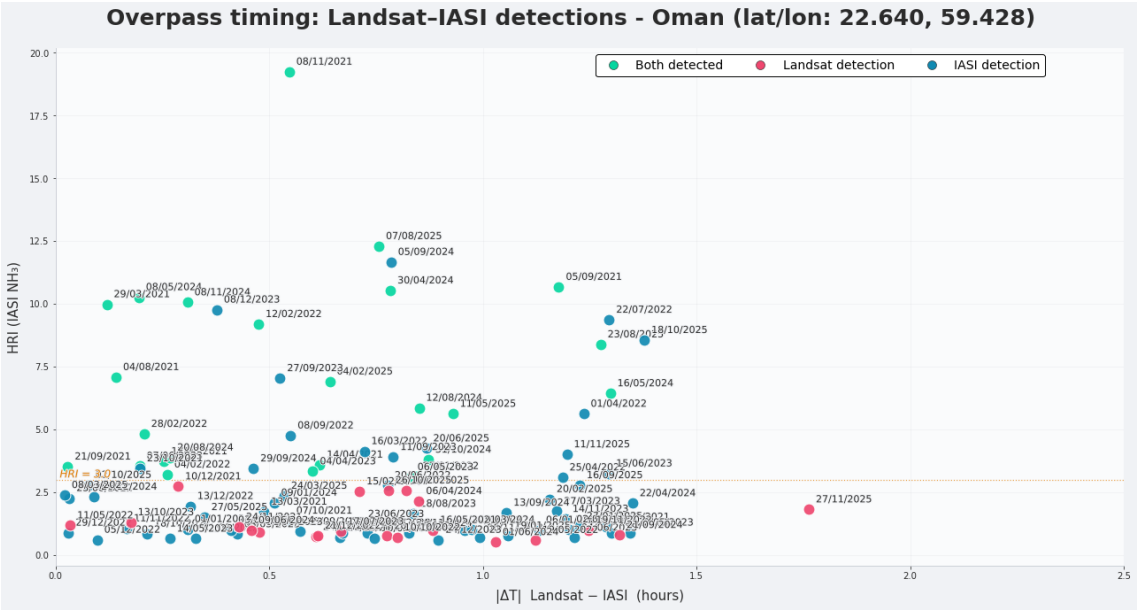


**Figure S13.** Scatter plot of IASI overpass timing versus the absolute Landsat-IASI time difference in the Oman fertilizer plant. Points are colored according to detection status: both sensors, Landsat only, or IASI only.

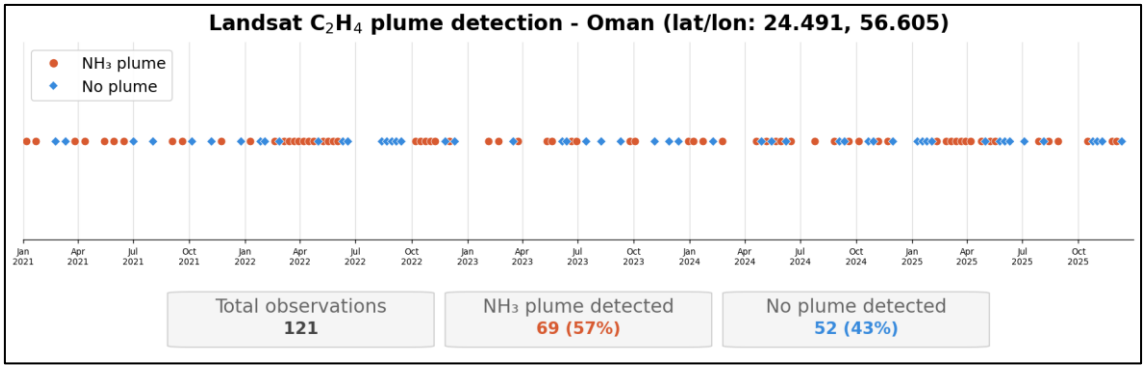


**Figure S14.** Detection timeline of all Landsat acquisitions between 2021-2025 in the Oman petrochemical plant, marking plume and no-plume days.

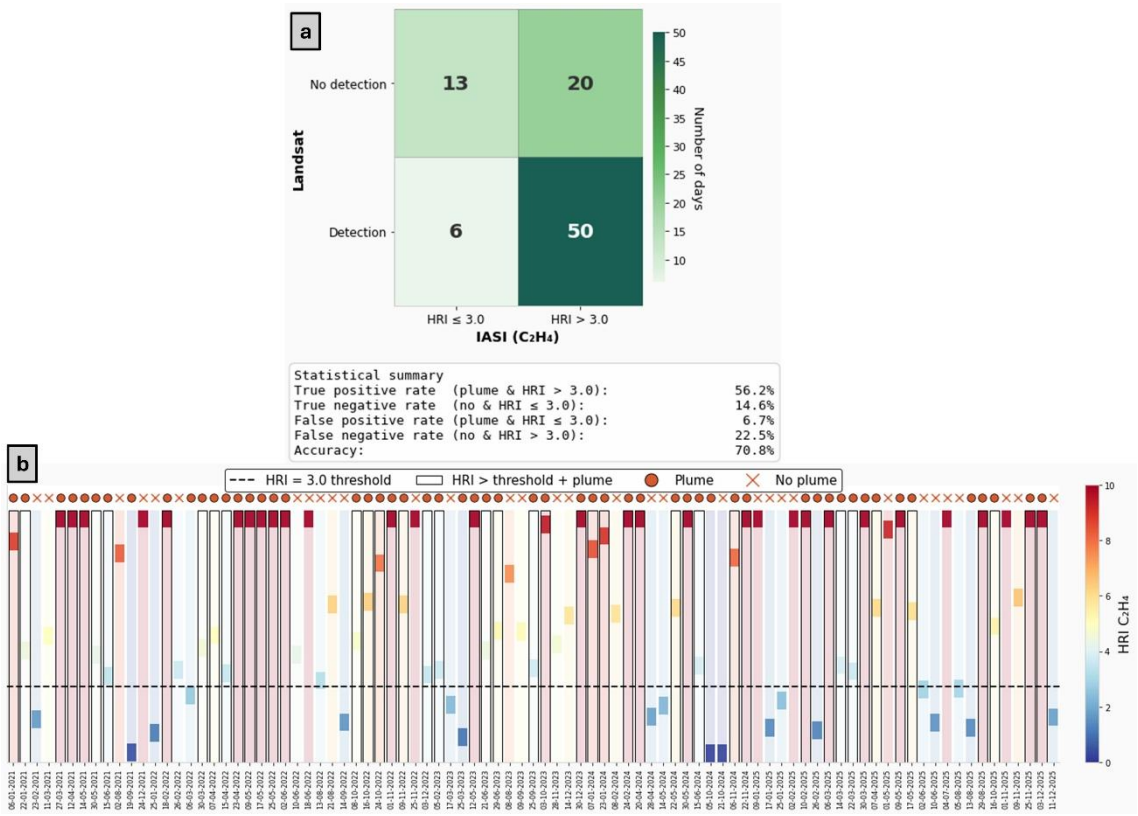


**Figure S15.** Landsat–IASI $NH_3$ comparison at the Oman petrochemical plant. (a) Confusion matrix of the Landsat plume flag against the IASI threshold (HRI > 3), with the true-/false-positive rates and overall accuracy. (b) Per-day IASI $NH_3$ HRI relative to the HRI = 3 threshold, with Landsat plume/no-plume markers.

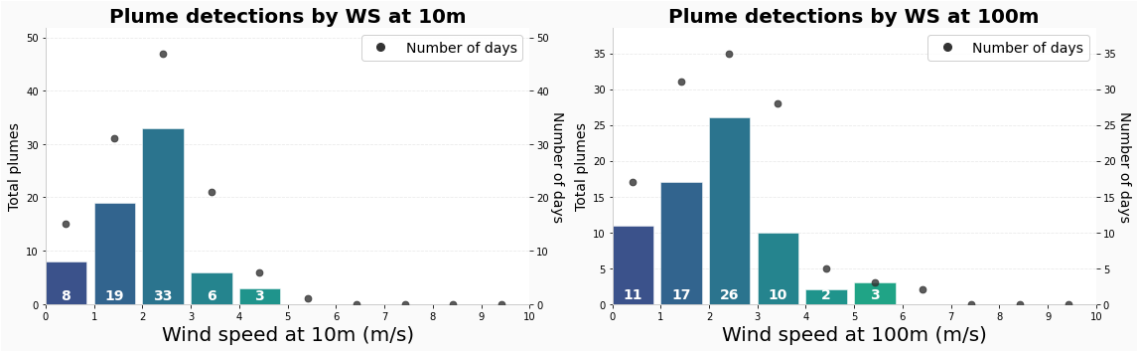


**Figure S16**. Plumes detected in the Oman petrochemical plant under different wind speed conditions at 10 m and 100 m.

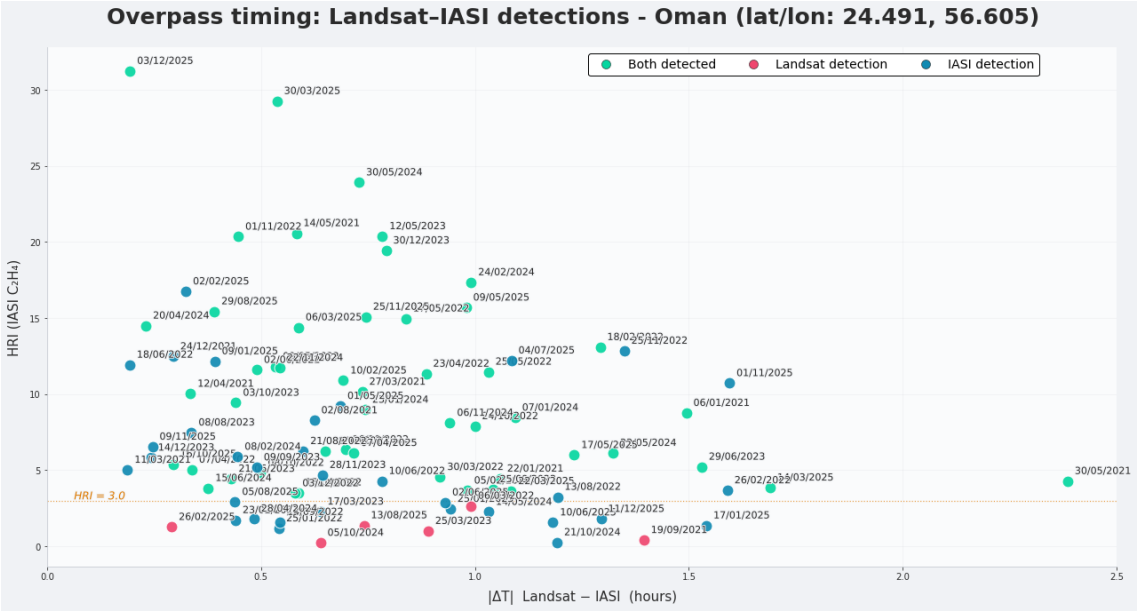


**Figure S17.** Scatter plot of IASI overpass timing versus the absolute Landsat-IASI time difference in the Oman petrochemical plant. Points are colored according to detection status: both sensors, Landsat only, or IASI only.

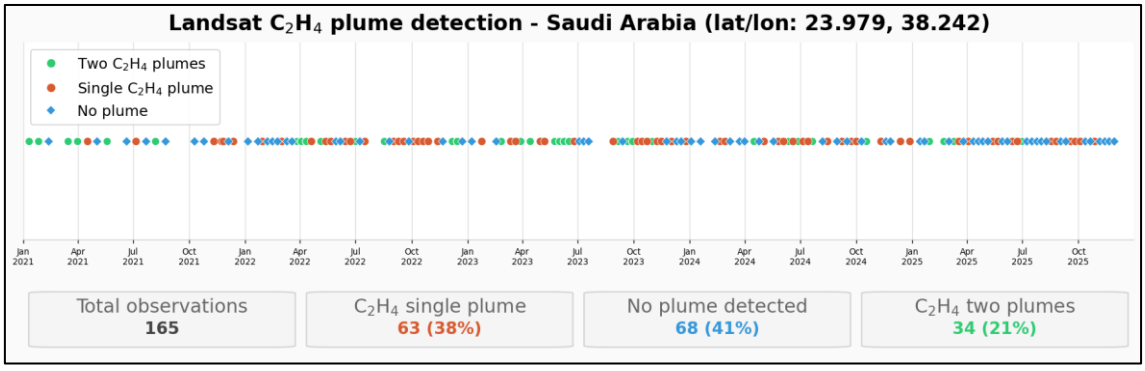


**Figure S18.** Detection timeline of all Landsat acquisitions between 2021-2025 in the Saudi Arabia petrochemical plants, marking plume and no-plume days.

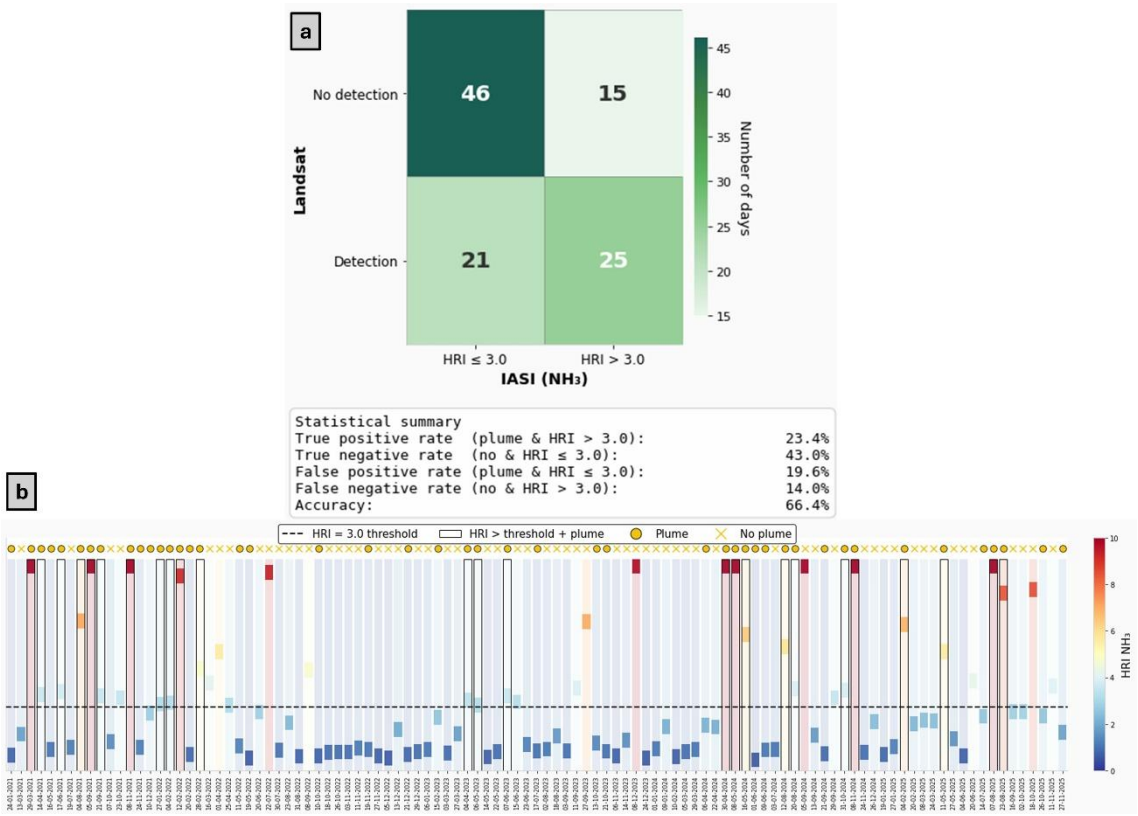


**Figure S19**. Landsat-IASI $NH_3$ comparison at the Saudi Arabia petrochemical plants. (a) Confusion matrix of the Landsat plume flag against the IASI threshold (HRI > 3), with the true-/false-positive rates and overall accuracy. (b) Per-day IASI $NH_3$ HRI relative to the HRI = 3 threshold, with Landsat plume/no-plume markers.

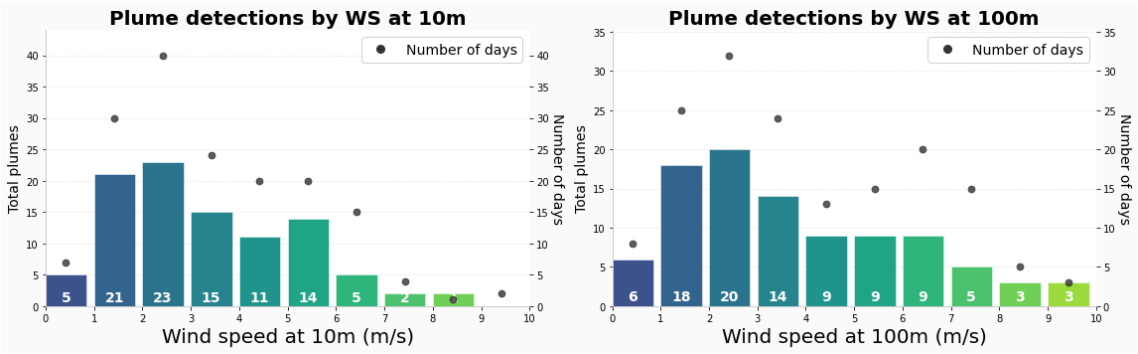


**Figure S20**. Plumes detected in the Saudi Arabia petrochemical plants under different wind speed conditions at 10 m and 100 m.

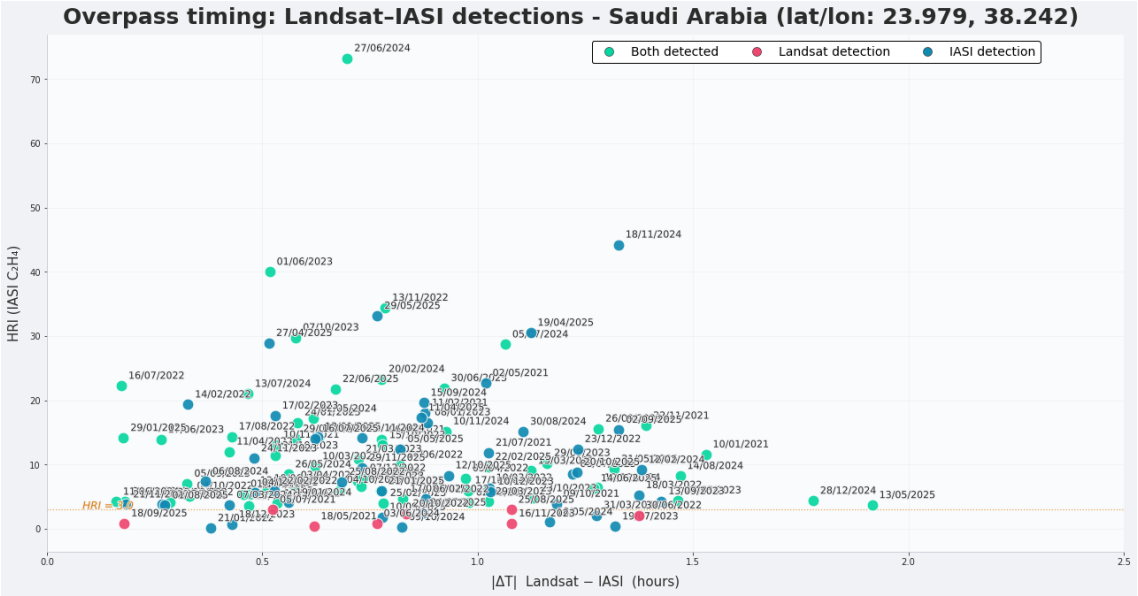


**Figure S21.** Scatter plot of IASI overpass timing versus the absolute Landsat-IASI time difference in the Saudi Arabia petrochemical plants. Points are colored according to detection status: both sensors, Landsat only, or IASI only.

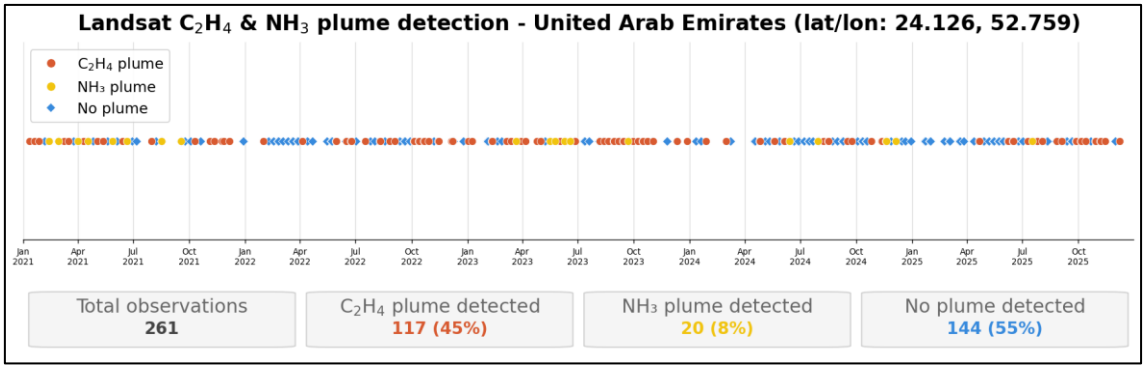


**Figure S22.** Detection timeline of all Landsat acquisitions between 2021-2025 in the United Arab Emirates complex, marking plume and no-plume days.

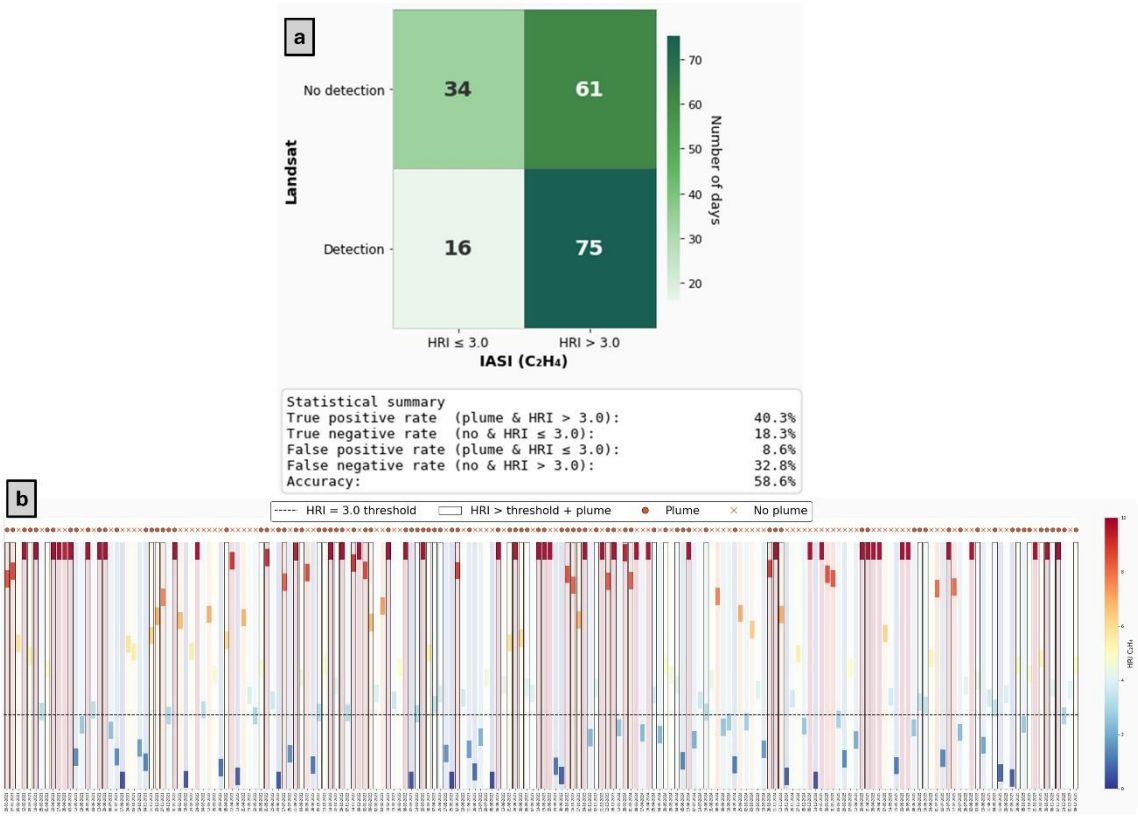


**Figure S23**. Landsat-IASI $NH_3$ comparison at the United Arab Emirates petrochemical plant. (a) Confusion matrix of the Landsat plume flag against the IASI threshold (HRI > 3), with the true-/false-positive rates and overall accuracy. (b) Per-day IASI $NH_3$ HRI relative to the HRI = 3 threshold, with Landsat plume/no-plume markers.

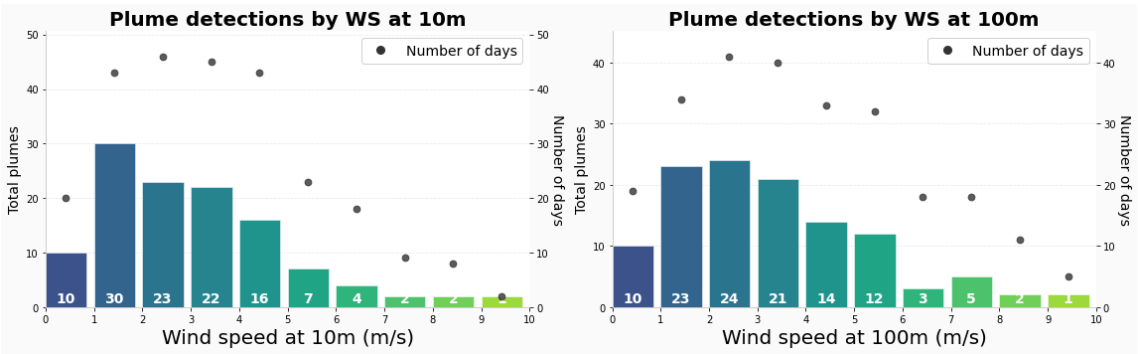


**Figure S24**. Plumes detected in the United Arab Emirates petrochemical plant under different wind speed conditions at 10 m and 100 m.

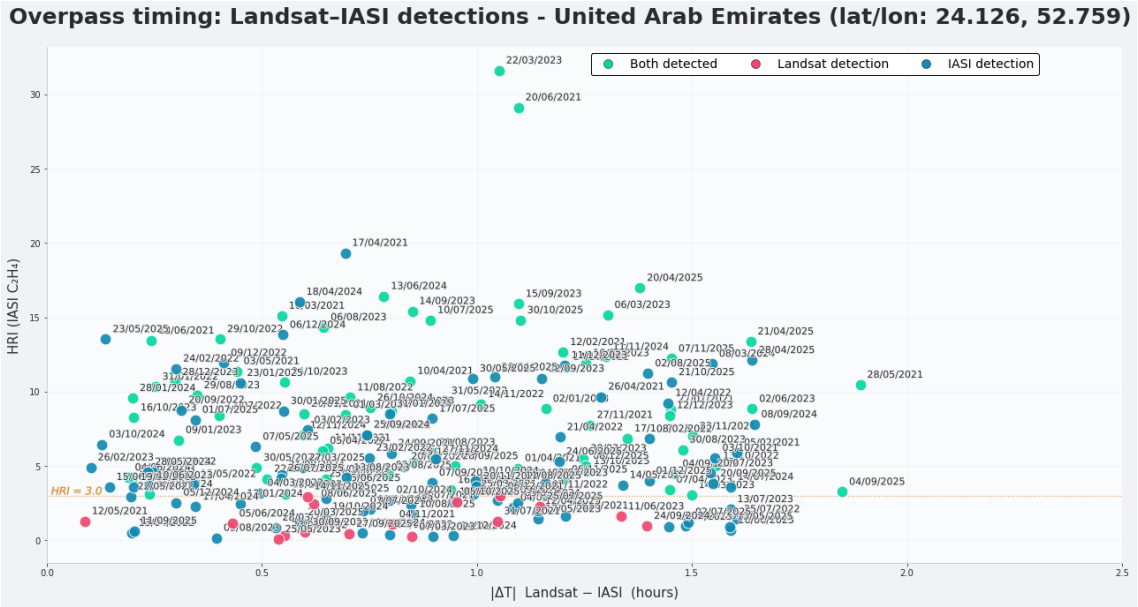


**Figure S25.** Scatter plot of IASI overpass timing versus the absolute Landsat-IASI time difference in the United Arab Emirates petrochemical plant. Points are colored according to detection status: both sensors, Landsat only, or IASI only.

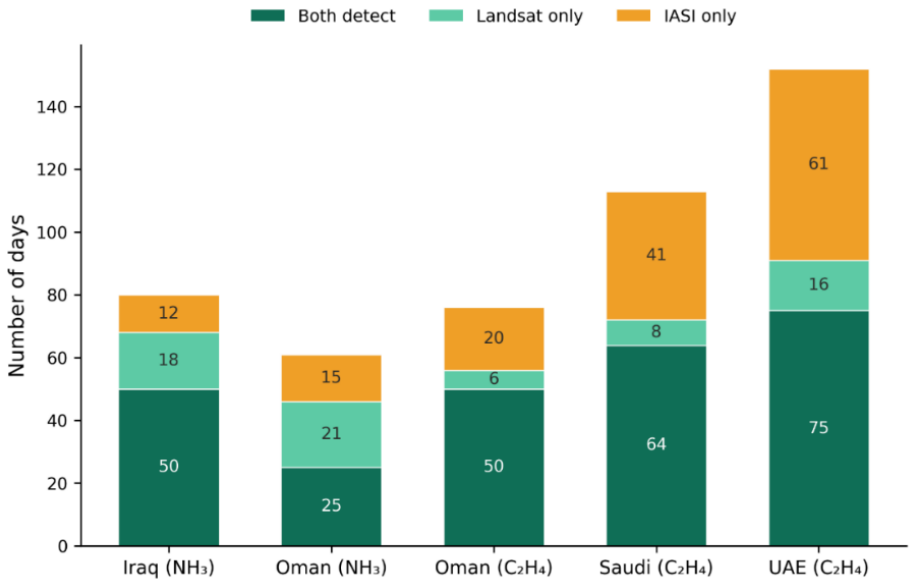


**Figure S26.** Cross-site comparison of Landsat–IASI detection agreement. Number of co-observed days at each of the five focus sources, partitioned into joint detections (both instruments, dark green), Landsat-only days (light green), and IASI-only days (orange). Joint detections dominate at every site, while the balance of the one-sided cases shifts with the source: Landsat-only days (sub-threshold IASI columns) are most frequent at the southern-Oman fertilizer plant, whereas IASI-only days (timing- or wind-driven misses) grow at the higher-throughput Saudi and UAE petrochemical sources.